The Synthesis and Study of Perovskites in Novel Forms

William Leal

A Thesis

in the Department

of

Chemistry & Biochemistry

Presented in Partial Fulfillment of the Requirements

For the Degree of Master of Science (Chemistry) at

Concordia University

Montreal, Quebec, Canada

December 2021

CONCORDIA UNIVERSITY

School of Graduate Studies

This is to certify that the thesis prepared

By: William Leal

Entitled: The Synthesis and Study of Perovskites in Novel Forms

and submitted in partial fulfillment of the requirements for the degree of

Master of Science (Chemistry)

complies with the regulations of the University and meets the accepted standards with respect to originality and quality.

Signed by the final examining committee:

_____ Chair

Dr. Yves Gélinas

_____ Examiner

Dr. Xavier Ottenwaelder

_____ Examiner

Dr. Rafik Naccache

_____ Thesis Supervisor

Dr. Marek B. Majewski

Approved by _____

Dr. Paul Joyce, Interim Chair of Chemistry & Biochemistry

_____

Dr. Pascale Sicotte, Dean, Faculty of Arts and Science

Abstract

The Synthesis and Study of Perovskites in Novel Forms

William Leal

The need for materials which aid in the production of clean energy has risen dramatically in recent years due to the looming threat of anthropogenic climate change. Perovskites have had a long history as a known material dating back to the 19th century and have seen an explosion of interest in the last 13 years as a material with great potential to oppose this threat when employed in devices for solar energy conversion. From the first perovskite-based photovoltaic to applications in photocatalysis, light emitting diodes, lasing, scintillation, and more, perovskite research moves on at a break-neck pace. Lead halide perovskites serve as the focus of much of this research as they possess unique optoelectronic properties which make them a prime candidate for application in solar energy conversion.

Though much work has been done to develop direct synthetic methods for producing lead halide perovskites, these methods offer little morphological variety, and it is well established that their optoelectronic properties are tied to their structure and morphology. As such, the present work aims to develop a synthetic procedure whereby $CaCO_3$ microstructures are electrochemically deposited on a transparent conducting oxide glass substrate and subsequently converted to $PbCO_3$ and then $CsPbBr_3$, resulting in stratified microstructures with a surface layer of $CsPbBr_3$ nanocrystals.

Lead halide perovskites also exhibit poor stability in the presence of moisture, which results in their degradation to PbX_2 salts which pose a risk to the environment. Metal halide double

perovskites of chemical formula $A_2BB'X_6$ have emerged as a lead-free alternative to lead halide perovskites, possessing a similar structure and comparable electronic properties. This thesis details the synthesis of $Cs_2NaYbCl_6$ as nanocrystals in order to merge the favorable optoelectronic properties of double perovskites with those associated with nanomaterials.

Acknowledgments

I'd first like to thank Dr. Marek B. Majewski for his insight, guidance, support, and lively discussion over the course of my work which helped me excel in my work and always aim for excellence. I thank my committee members Dr. Xavier Ottenwaelder (Dr. X) and Dr. Rafik Naccache for their help and useful advice on my research. I thank all my wonderful lab-mates Joey Ricardo-Noordberg, Zujhar Singh, Francisco Yarur Villaneuva, Caroline L. Bergeron, Rehmat Brar, Jacob Hui, Victoria Lapointe, Linyi Wei, and the Howarth group for supporting me and helping me learn, grow, and laugh as a researcher. I also thank Tyler J. Rutherford for his help in assisting me with a part of the synthetic procedure of the project.

I thank the Natural Sciences and Engineering Research Council of Canada (NSERC), the Fonds de Recherche du Québec – Nature et technologies (FRQNT) and the Quebec Centre for Advanced Materials (QCAM) for financial support. SEM-EDS data was acquired at the Centre for Characterization and Microscopy of Materials (CM^2). DRIFTS data was acquired at the Integrated Platform for Biomolecular Function, Interactions and Structure (BIOFINS). Fluorescence microscopy images and videos were acquired at the Centre for Microscopy and Cellular Imaging (CMCI) with the help of Dr. Chris Law. ICP-MS data was acquired at the Centre for Biological Applications of Mass Spectrometry (CBAMS) with the help of Dr. Heng Jiang. PXRD data was acquired at the McGill Chemistry Characterization (MC^2) centre with the help of Dr. Hatem Titi. DRS data was acquired at the Laboratoire d'Analyse des Molécules et des Matériaux Photoactifs (LAMP) with the help of Dr. Daniel Chartrand.

I'd like to thank all my friends for their love and support over the years, especially Joseph and Bradley "Bob" Steen. Thank you to Paola Marino, Zvart Ajoyan, Hudson Bicalho, Victor Quezada, Chris Copeman, Amna Muhammad, Samantha Prelaz, Lars Miller, Ximena Canales and

all the undergrads for making my graduate school experience one to remember and cherish. Finally, I'd like to thank Thomas O'Malley for the background vocals.

Dedications

I dedicate this work to my dearest friend Alyssa "Lily" Penney for being an amazing human to talk and spend time with, to Evan Fruchthandler for inspiring in me a love for chemistry that I'll always take with me, to my best friend and love Caroline Bergeron for always believing in and encouraging me, and to my parents who provided for and supported me all my life so I could achieve this goal. I love you all.

Contribution of Authors

Marek B. Majewski acted in a supervisory role in all chapters of this work. In Chapter 2, Tyler J. Rutherford performed the work regarding the electrochemical deposition of $CaCO_3$ for different amounts of time. Caroline L. Bergeron collected TEM micrographs and associated data in Chapters 2 and 3. I performed all other experimental work and characterization. Chapter 2 has been published as a preprint and I am the principal author of this work. I am also the principal author of Chapter 3.

Publications arising from this work:

Leal, W.; Bergeron, C.; Rutherford, T.; Majewski, M. Conversion of Electrochemically Deposited Aragonite Crystallites to Perovskite through In Situ Ion Exchange. *ChemRxiv* **2021**. This content is a preprint and has not been peer-reviewed.

Table of Contents

List of Figures

List of Tables

List of Abbreviations

1D	One-dimensional
2D	Two-dimensional
3D	Three-dimensional
AES	Auger Electron Spectroscopy
BCCP	Bacterial Calcium Carbonate Precipitation
CCP	Calcium Carbonate Precipitation
DIC	Dissolved Inorganic Carbon
DP	Double Perovskite
DPE	Diphenyl Ether
DRIFTS	Diffuse Reflectance Infrared Fourier-Transform Spectroscopy
DRS	Diffuse Reflectance Spectroscopy
EDS	Energy Dispersive X-ray Spectroscopy
FA	Formamidinium
FM	Fluorescence Microscopy
FTO	Fluorine-doped Tin Oxide
HOMO	Highest Occupied Molecular Orbital
HR-TEM	High Resolution Transmission Electron Microscope
HTM	Hole Transport Material
ICP-MS	Inductively Coupled Plasma Mass Spcetrometry

JDOS	Joint Density of States
LED	Light-Emitting Diode
LMCT	Ligand-to-Metal Charge Transfer
LUMO	Lowest Unoccupied Molecular Orbital
MA	Methylammonium
MHP	Metal Halide Perovskite
MMCT	Metal-to-Metal Charge Transfer
NC	Nanocrystal
OA	Oleic Acid
ODA	Octadecylammonium
ODE	Octadecene
OLAM	Oleylamine/Oleylammonium
PL	Photoluminescence
PNC	Perovskite Nanocrystal
PXRD	Powder X-ray Diffraction
RCF	Rotational Centrifugal Force
RPM	Rotations Per Minute
SEM	Scanning Electron Microscope
TBA	Tetrabutylammonium

Chapter 1: Introduction

1.1 Metal Carbonates

A plethora of metal carbonates can be found in nature either as minerals or as part of ores. Minerals such as magnesite ($MgCO_3$, trigonal), calcite ($CaCO_3$, trigonal), strontianite ($SrCO_3$, orthorhombic), witherite ($BaCO_3$, orthorhombic), cerussite ($PbCO_3$, orthorhombic), siderite ($FeCO_3$, trigonal), and smithsonite ($ZnCO_3$, trigonal) are naturally occurring, each with their own uses in society.[1] While mining remains a common practice for extracting these materials, a great deal of interest in the scientific community has been placed on understanding how they are produced in nature so that those processes might be synthetically mimicked. To that end, biomineralization, the generation of minerals by living organisms, is a process that has garnered much attention as an avenue for achieving this goal. Calcium carbonate, specifically, is a mineral attracting much attention in this regard as it is made by countless organisms, including humans, in various morphologies. Calcium carbonate has three naturally occurring crystal structures, calcite (trigonal), aragonite (orthorhombic), and vaterite (hexagonal), with calcite being the most thermodynamically stable polymorph and vaterite the least (Figure 1.1).

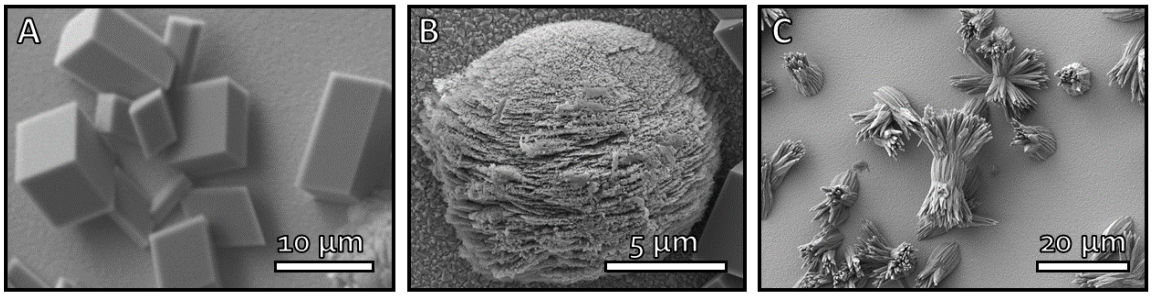

Figure 1.1: Scanning electron micrographs of the three naturally occurring polymorphs of $CaCO_3$, (A) calcite (trigonal), (B) vaterite (hexagonal), (C) aragonite (orthorhombic).

1.1.1 Formation of Calcium Carbonate in Nature

It is well known that calcium carbonate ($CaCO_3$) is a ubiquitous compound which is produced on a variety of scales in nature. It is produced by bacteria in bacterial calcium carbonate precipitation (BCCP) in many different biomes including ocean water and sediments, freshwater, and soils.[2-3] Calcium carbonate precipitation (CCP) is a process dependent on four key factors: Ca^{2+} concentration, dissolved inorganic carbon (DIC) concentration, pH, and nucleation site availability.[4] The way in which bacteria have been primarily reported to induce BCCP is in controlling the pH and DIC concentration, either actively or passively, by various physiological processes, though the exact nature of this process is a subject of intense debate.[2, 5]

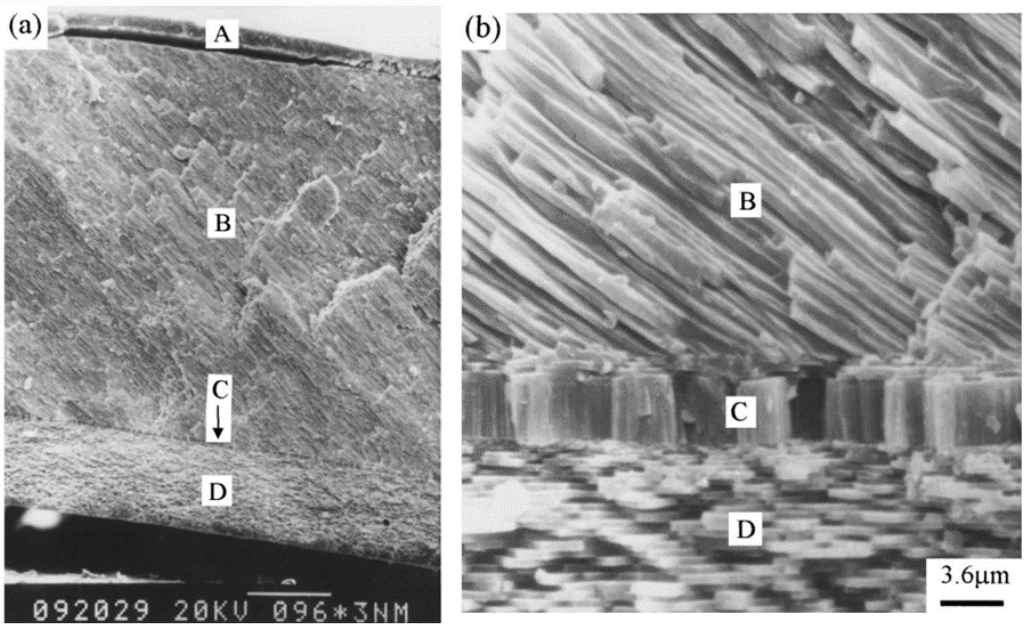

Figure 1.2: Scanning electron micrographs of (a) the morphology of the cross-section of the shell of *Mytilus edulis*, the blue mussel (A: periostracum, B: oblique prismatic layer, C: normal prismatic layer, D: nacreous layer). (b) Amplified image of (a) showing the structure of the oblique prismatic layer (reprinted with permission from ref. 7).

Calcium carbonate is also produced by countless aquatic organisms as a structural component in shells, spines, claws, scales, and eye lenses. Even different terrestrial organisms

produce it for use in eggshells, inner ears, or as calcium deposits in the case of some plants.[6] These larger-scale organisms each possess their own method for producing calcium carbonate for their different uses, and many of these processes are not yet known, such as how molluscs produce the two different layers of calcium carbonate in their shells. Mollusc shells are composed almost exclusively of calcium carbonate, the outer layer being made of calcite, and the inner layer, called nacre, being made of aragonite (Figure 1.2). Though it is known that switching of the two polymorphs is controlled by a thin layer of cells called the outer epithelium, the exact way in which they do so is still unknown.[6-7] However, this has not prevented scientists from attempting to synthetically replicate the production of these fascinating materials.

1.1.2 Synthetic Accessibility of Morphologies

Over the years there have been many methods developed for the synthesis of calcium carbonate in different morphologies. The most rudimentary methods involve crystallization with the incorporation of ion additives such as Fe^{3+}, Mg^{2+}, Ni^{2+}, Co^{2+}, Zn^{2+}, and Cu^{2+} to favour the formation of a specific polymorph like aragonite.[8] Other parameters of crystallization can be varied as well such as temperature and pH. Adding molecules like amino acids has also been explored in order to synthesize chiral calcium carbonate crystals. Adding macromolecules, such as fatty acids and stearic acid, has been extensively studied for controlling all aspects of calcium carbonate growth from crystal nucleus size and growth rate to preferred polymorph formation.[9]

Electrochemical deposition is a technique which offers many advantages over traditional crystallization methods. It can be performed in much shorter periods of time, with great reproducibility and allows for the material to be preferentially deposited directly onto the substrate. This method also allows for a greater degree of parametric control, where the applied bias or deposition substrate surface can be varied in addition to conventional parameters of crystal growth

such as temperature, ion concentration, and pH.[10-11] The electrochemical deposition of $CaCO_3$ operates by applying a negative bias across a working electrode, triggering a two-electron reduction of water as per Equation 1:[12]

$$H_2O + 2e^- \rightleftharpoons H_2 + OH^- \quad (1)$$

$$OH^- + Ca^{2+} + HCO_3^- \rightleftharpoons CaCO_3 + H_2O \quad (2)$$

This produces hydroxide ions at the working electrode (cathode) which react with in-solution HCO_3^- ions to form carbonate anions, which subsequently react with Ca^{2+} ions to form $CaCO_3$ on the electrode surface.[13] The morphology of the resultant crystallites can be controlled by varying parameters of the deposition, for example the presence of Mg^{2+} ions and increased temperature hindering the growth of calcite and favouring aragonite, or chiral amino acids as additives to produce chiral calcite microstructures.[12] Electrochemical deposition is a powerful tool for harnessing calcium carbonate's remarkable ability as a morphological template, which is often observed in nature.

1.2 Nanomaterials

In recent years a great deal of interest has been shown in the scientific community towards the synthesis of nanoscale materials. This can be seen in a variety of fields such as electronics,[14-15] solar energy conversion,[16-18] drug delivery,[19] and medical treatment,[20] each benefitting from different aspects of nanomaterials and their various advantages. A material is generally considered a nanomaterial when it measures 100 nm or less in at least one dimension, such as a nanowire (1D), nanosheet (2D), or nanoparticle (3D). In the field of solar energy conversion, where there is a specific focus on the synthesis of photocatalytic materials, their facile and tunable synthesis,

large surface area-to-volume ratio, and tunable optical properties are all advantageous properties.[21-22]

1.2.1 Synthesis

Nanomaterials can be synthesized by top-down or bottom-up synthetic methods.[23-24] A top-down approach entails decomposing or deconstructing a bulk material down to the nanoscale to obtain a nanomaterial. Bottom-up synthesis, on the other hand, involves a chemical reaction which produces a nanosized material. Parameters such as reagent concentration, reaction temperature, addition of reaction-mediating or structure-directing surfactants, and reaction time can all be tuned to produce a product with a desired physical or structural property. Which approach is best for the synthesis of a particular nanomaterial is dependent on the material and its intended application. It has been shown that both bottom-up and top-down synthesis can result in materials nearly indistinguishable from one another.[25-26] In the case of nanocomposite formation, however, bottom-up synthesis allows the combination of metals like cobalt and bismuth which are immiscible by other synthetic means.[27] Top-down synthesis, on the other hand, can be of great use in cases where high throughput is needed, such as for the synthesis of graphene quantum dots.[28]

1.2.2 Surface Area-to-Volume Ratio

As a material's dimensions are reduced from the bulk scale to the nanoscale, the surface area-to-volume ratio of the material increases as the volume of the material decreases by a factor of 10^3 while the surface area decreases by a factor of 10^2. This is illustrated in Figure 1.3 where a cube of edge length l = 5 cm is compared to 125 cubes with edge length l = 1 cm. Both examples exhibit the same total volume, however the collection of smaller cubes has much more surface area exposed compared to if they were all put together in a single cube. This makes it so more of the material is part of a surface and made available for surface interactions, which is beneficial for

applications such as photocatalysis, a pillar of solar energy conversion. It has been shown that increased surface area of a material can improve its photocatalytic ability, as more of the material is exposed to the reaction solution.[29]

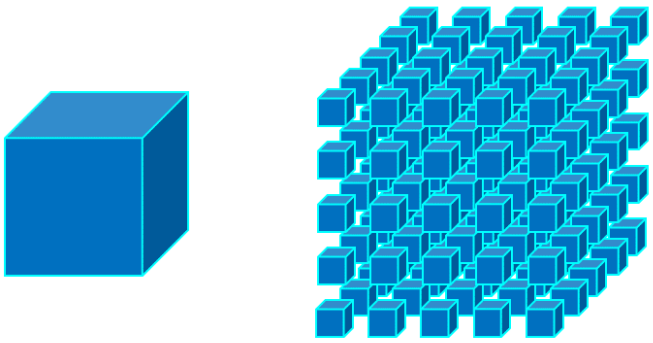

Figure 1.3: Volume and surface area of one cube with dimensions 5 × 5 × 5 cm vs. 125 cubes with dimensions of 1 × 1 × 1 cm.

1.2.3 Size-dependent Properties

At the nanoscale, the electronic structure, optical, and magnetic properties of the material become dependent on particle size, as dictated by the quantum confinement effect. The quantum confinement effect occurs when the size of a particle approaches the exciton Bohr radius. At this scale, the continuum of energy levels for an electron confined in the particle becomes discrete, making it so the solution for the electron energy from Schrodinger's equation is:

$$E_n = \frac{h^2 n^2}{2 m_e L^2} \quad (3)$$

This shows that the electron energy E_n is inversely proportional to the particle size L, which explains why decreasing particle size causes a blue-shift in emission, and results in an increase in

bandgap energy. This has been shown in previous work and has since been the driving force for designing new materials or previously existing ones as nanomaterials for use in light-based devices such as light-emitting diodes (LEDs), photovoltaic cells, and lasers.[30-32] The size dependence of these properties enables another method in which a synthesized material can be fine-tuned for its application. For example, metal halide perovskite nanocrystals (MHP NCs) are a material which take full advantage of this property by way of controlling the NC size to tune the bandgap energy, allowing them to span the entire visible spectrum without need for changing the chemical composition.[33]

1.3 Perovskites

Perovskites are a class of semiconducting material with the general chemical formula ABX_3 (A = monovalent cation, B = divalent cation, X = monovalent anion), crystallizing in a cubic crystal unit cell with BX_6 corner-sharing octahedra and belonging to the $Pm\bar{3}m$ space group (Figure 1.4A).[34] Many variations of perovskite exist and do not necessarily follow this strict definition. Most perovskite materials do not crystallize in a perfect cubic crystal system, often exhibiting distortions in the network of BX_6 octahedra as they individually tilt due to differences in size of the different A, B, and X ions.[34] $CaTiO_3$, the first perovskite found in 1839,[35] exhibits such a distorted cubic structure. However, materials such as these have their BX_6 octahedron network intact, so they are considered hettotypes (structures similar to the aristotype of a group of crystal structures but with lower symmetry) of the perovskite aristotype (the structure with the highest symmetry in a group of crystal structures).[34] Though $SrTiO_3$ (tausonite) is generally considered to be the perovskite aristotype, it does not crystallize in a perfect cubic perovskite crystal system.[34] In fact, that honour belongs to $KMgF_3$ (paraschondolaite), one of the few naturally occurring perovskites, which crystallizes in a perfect cubic crystal system, making it

more suitable for consideration as the perovskite aristotype.[36] More extreme instances of octahedron network distortion lead to orthorhombic or tetragonal perovskite crystal systems (Figure 1.4B, C).[37] Variations of the chemical formula ABX_3 can be made and still qualify as perovskite structures as well, as in the case of double perovskites (DPs), with chemical formula $A_2BB'X_6$ such as $Cs_2BiAgCl_6$,[38] and vacancy-ordered perovskites in which vacancies replace the A-and/or B-site cation.[39]

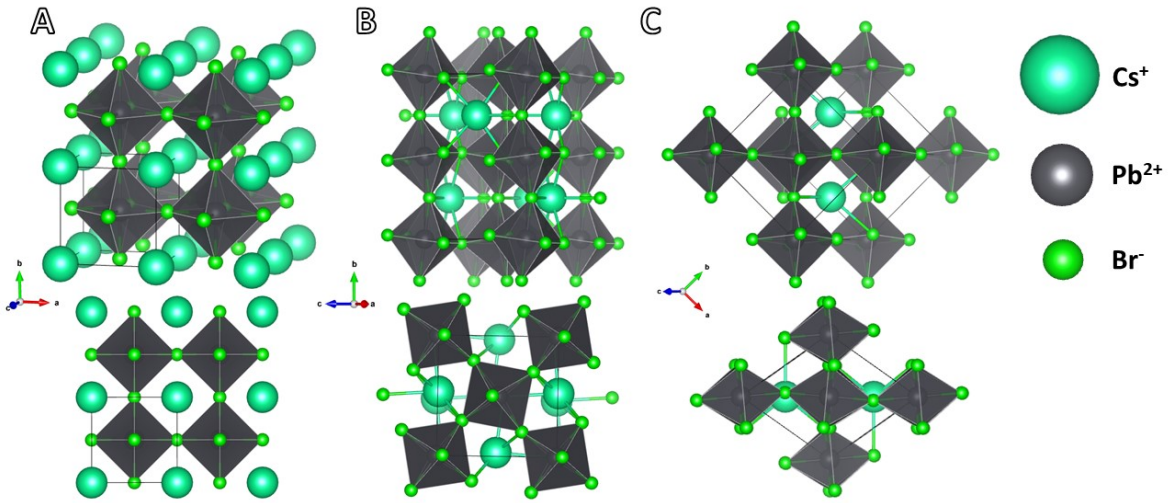

Figure 1.4: Cesium lead bromide in its three possible perovskite phases, (A) cubic (ICSD 29073), (B) orthorhombic (ICSD 97851), and (C) tetragonal (ICSD 109295) with their accompanying head-on views.

1.3.1 Major Categories of Perovskite

Within the larger family of perovskites, there are several divisions and categories that exist. The two major categories are halide and oxide perovskites, where X will either be a halide, as in $CsPbBr_3$, or oxygen, as with $CaTiO_3$, respectively. These categories can be further divided into metal and non-metal halide/oxide perovskites and divided further still into all-inorganic or hybrid organic-inorganic. The present work is focused on MHPs as they have been of extreme interest in

the field of solar energy conversion in the last decade due to their excellent optoelectronic properties.

1.3.2 Hybrid Organic-Inorganic Perovskites

Though perovskite research dates to the 19th century, it was not until the 21st century that they garnered attention as an outstanding material for various light-based applications. Originally, perovskite was the name given to $CaTiO_3$ in 1839 but was later used in 1926 to name the family of compounds sharing its crystal structure such as $BaTiO_3$, $SrTiO_3$, and $BiFeO_3$.[40] These perovskite oxides, and many more like them, continued to dominate perovskite research throughout the 20th century for their interesting electronic and magnetic properties but did not possess the properties needed to revolutionize the field of solar energy conversion. This is mainly a product of their electronic structures resulting in large bandgaps not suitable for harvesting sunlight.[41] However, discoveries are still being made today, as in the case of $CaSiO_3$ (davemaoite) which was just discovered encased in a diamond which came from the Earth's lower mantle and bears importance as a mineral which helps influence the heat budget of the deep mantle.[42] Furthermore, a branch of perovskite oxide research has taken on adapting these materials to make them suitable for solar energy conversion applications like photocatalytic CO_2 reduction.[43]

MHPs can trace their discovery to 1893 with the first synthesis of $CsPbX_3$,[44] but weren't classified as materials with perovskite structure until 1957,[45] and it was not until 1978 that the first hybrid organic-inorganic perovskites, $CH_3NH_3MX_3$ (M = Pb, Sn, X = Br, I), were synthesized.[46-47] Only in 2009, however, was the light-harnessing potential of halide perovskites truly unlocked in the first reported perovskite-based photovoltaic device.[48] $CH_3NH_3PbX_3$ has since led the charge in pushing perovskite science to new heights as a high-performing semiconducting material with excellent optoelectronic properties. Hybrid halide perovskites boast electronic structures that result

in long charge carrier diffusion lengths, low exciton binding energies, strong light absorption in the visible light regime, and tunable bandgap energies.[49] They are also solution-processable and can be made from inexpensive materials. Current top iterations of the hybrid organic-inorganic MHP contain A-site organic cations that are either methylammonium ($CH_3NH_3^+$, MA) or formamidinium ($CHN_2H_4^+$, FA) and Pb as the B-site metal cation (although much research is done with Sn and Ge as the B-site cation as well).[34, 50-53]

Though these materials have been at the forefront of perovskite research towards application in light-based processes, they suffer from poor stability, both intrinsic and extrinsic. Perovskites are prone to ion migration, which can contribute to deterioration of the crystal structure and, subsequently, the material's optoelectronic properties.[54] Even more serious is the issue of poor stability in the presence of ambient heat and humidity, whereby a degradation pathway is triggered resulting in insoluble PbX_2, posing a serious environmental hazard.[55-57] This has driven scientists to focus efforts on circumventing these issues, either by stabilizing the material, such as with the use of passivating capping groups, or by synthesizing new, lead-free perovskites.

1.3.3 All-inorganic Metal Halide Perovskites

Much like their hybrid counterparts, all-inorganic perovskites are a material that, despite being known for many years, only saw a surge of interest in the last decade. This surge was intensified when Protesescu *et al*. reported the first synthesis of $CsPbX_3$ colloidal nanocrystals.[33] This study was of monumental importance not only for having shown that the material's bandgap energy could be tuned to span the entire visible light regime, but for developing a synthesis resulting in colloidally stable all-inorganic MHP NCs which would be adapted for synthesizing many other such materials.[58-60]

One of the reasons for the recent popularity of these materials is their improved stability over that of hybrid organic-inorganic perovskites. All-inorganic perovskites have a large metal cation (e.g., Cs^+) as their A-site cation which is less solvated by water than the weakly bonded organic A-site cations, such as MA and FA, used in hybrid perovskites. This improved stability, coupled with the fact that all-inorganic halide perovskites have comparable electronic properties to their hybrid counterparts, especially $CsPbX_3$, makes them a viable replacement for use in solar energy conversion over hybrid perovskites.

1.3.4 Optoelectronic Properties

MHPs possess desirable optoelectronic properties as semiconductors. One of their defining properties is their high light absorption cross-section, which, in addition to generally possessing a direct bandgap, is due to the nature of the transition at the band edge. This transition arising from the halide *p*-orbital to the metal *p*-orbital enhances the optical absorption, as *p*-orbitals exhibit less dispersion than *s*-orbitals which is reported as resulting in a larger joint density of states (JDOS).[49] As such, better overlap between the halide and metal *p*-orbitals results in increased absorption, and the overlap is dependent on the B-X-B bond angle in the crystal structure of the material. An angle of $\theta = 180°$ results in a perfect cubic structure, and optimal orbital overlap resulting in improved electronic properties.[37] As this angle decreases, the BX_6 octahedra tilt to the detriment of the orbital overlap and, subsequently, the material's electronic properties. This contributes to the crystal structure of the material going from cubic to orthorhombic to tetragonal, however these are still considered perovskite phases as the octahedron network is still intact,[34] though now at a sub-optimal angle θ. It is interesting to note that the A-site cation does not directly impact the material's electronic properties but, rather, can cause octahedron tilting due to its size and how it fits into the crystal lattice.[37, 61]

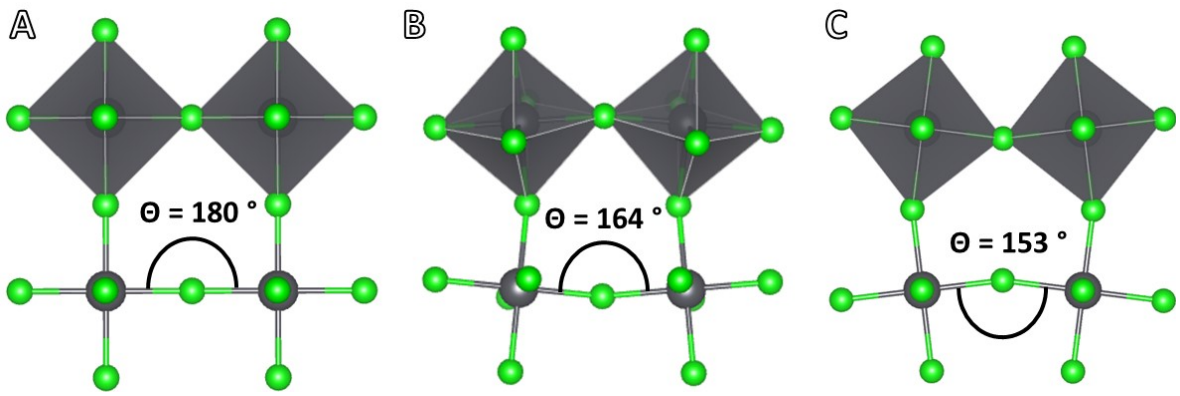

Figure 1.5: M-X-M bond angle θ in metal halide perovskite with (A) cubic, (B) orthorhombic, and (C) tetragonal crystal unit cell.

Other electronic properties for which MHPs are celebrated, such as long charge carrier diffusion lengths and low exciton binding energy, arise partially due to their rare tolerance to forming electronic defects. These defects can occur as vacancies in the crystal lattice or Schottky-type defects and can create defect energy levels which can interfere with the material's electronic transitions and properties.[62] In the case of MHPs, their tolerance to such defects lies in the fact that these energy levels generally reside in the valence or conduction band, preserving the nature of the bandgap.[63] Though this is noted as a tolerance and not an immunity, it does result in MHPs being a very electronically robust material. However, this has not stopped scientists from attempting to improve the defect tolerance further still, i.e., *via* the incorporation of organic capping groups on the surface to passivate the material and render it less susceptible to the generation of defects. This is typically done using pairs of long chain organic like oleylamine and oleic acid, which enter an equilibrium in solution to form a positively and negatively charged group, respectively.[33, 64] However, work is being done to ascertain new molecules which can more effectively perform this task and even potentially enhance the base material's electronic properties.[65-67]

1.3.5 Tunable Bandgap

One of the strengths that MHPs have is their tunable bandgap which renders them a very versatile material. It was shown in the pioneering work done by Protesescu *et al.* that all-inorganic MHPs could be synthesized in such a way that their bandgap energy could be tuned to any point in the visible light regime (Figure 1.6).[33] This was done not only by demonstrating the synthesis for the three different halides, $CsPbX_3$ (X = Cl, Br, I), but also for mixed halide perovskites, $CsPb(Cl/Br)_3$ and $CsPb(Br/I)_3$. In adjusting the ratio of halide precursors, PbX_2, when performing the synthesis, one can tune the photoluminescence (PL) of the material to any part of the visible spectrum.

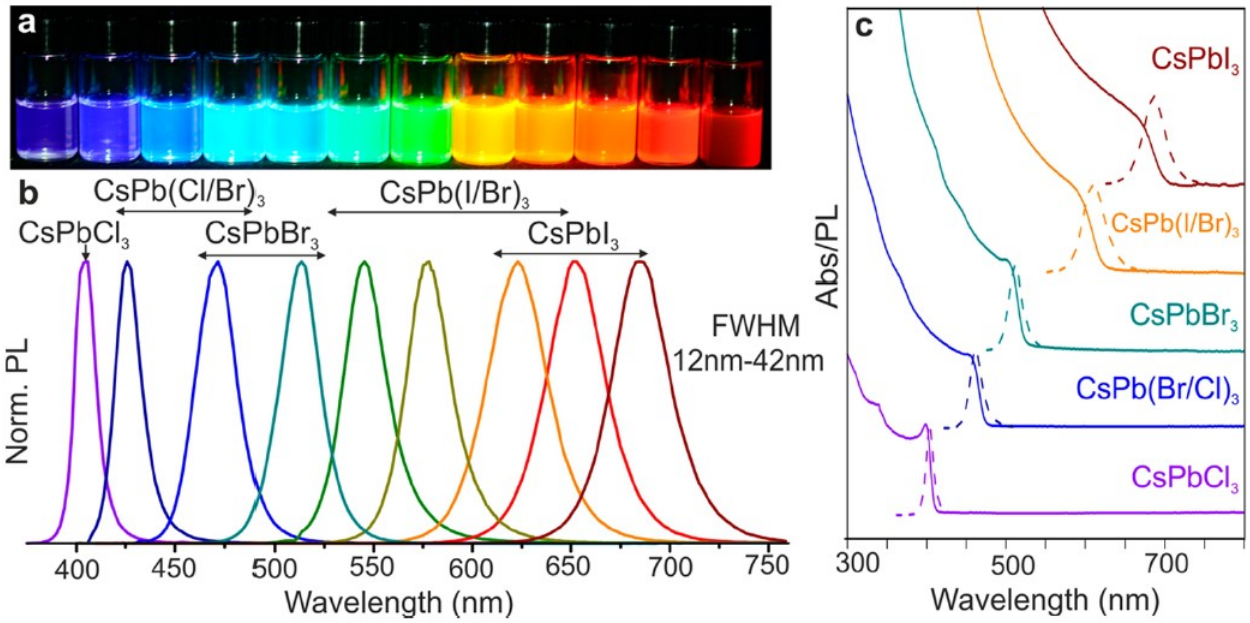

Figure 1.6: Colloidal perovskite $CsPbX_3$ NCs (X = Cl, Br, I) exhibit size- and composition-tunable bandgap energies covering the entire visible spectral region with narrow and bright emission: (a) colloidal solutions in toluene under UV lamp (λ = 365 nm); (b) representative PL spectra (λ_{ex} = 400 nm for all but 350 nm for $CsPbCl_3$ samples); (c) typical optical absorption and PL spectra (reprinted with permission from ref. 33).

Later work done by Akkerman *et al.* and Nedelcu *et al.* showed that post-synthetic modification of the MHP NC chemical composition was a possibility as well by exposing their

synthesized $CsPbX_3$ NCs to a variety of halide-containing reagents.[68-69] Reagents of note were oleylammonium halides (OLAM-X), lead halide salts (PbX_2), octadecylammonium halide (ODA-X), and tetrabutylammonium halide (TBA-X). The latter three saw lesser degrees of anion exchange, with PbX_2 and ODA-X taking much longer to perform the exchange due to their insolubility, and TBA-X only working to exchange Br^- and I^- for Cl^- and Br^-, respectively, but not the inverse. OLAM-X, however, proved to be very effective in converting the NCs in a matter of seconds. The conversion was even performed by mixing MHP NCs of different halides to obtain mixed halide perovskites. The ratios here, too, could be adjusted to control the resulting ratio of the solid solution material.

1.3.6 Limitations

Aside from the underlying issue of perovskite stability discussed in Section 1.3.3, MHPs have another shortcoming in that they offer little morphological variety. NCs have been shown to be synthesized as nanocubes, nanosheets/platelets, or nanorods but offer little else in the way of morphology despite their facile and direct synthesis.[70-71] This is true in the bulk scale as well, where MHPs have been shown to only crystallize in a handful of morphologies,[72-74] and this presents one avenue of research which might result in further tuning the properties of this already versatile material for use in applications such as photocatalysis for solar energy conversion.

1.4 Double Perovskites

While an "ideal" definition of a perovskite does exist, there are many different materials that fall into this broad category of semiconductor. Double perovskites (DPs) are one such material that has also garnered much interest in recent years. As perovskites have the general chemical formula ABX_3, doubling this formula results in a chemical formula of $A_2B_2X_6$. This, of course, is

a redundant action; however, upon substituting the divalent B-cation for a monovalent and trivalent cation, B and B' respectively, one is left with a chemical formula of $A_2BB'X_6$, hence the name double perovskite (Figure 1.7).

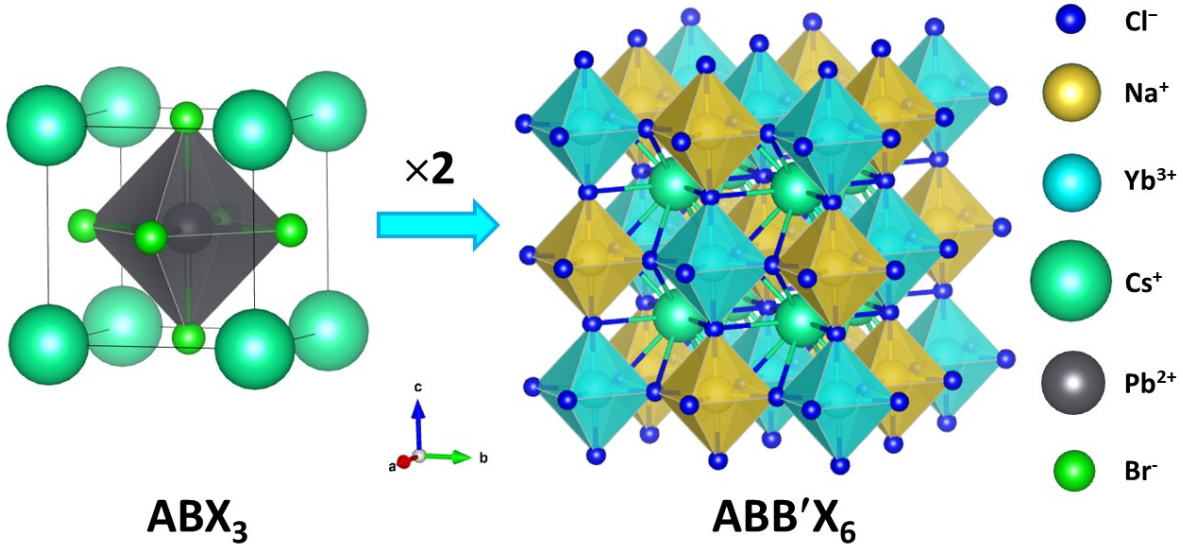

Figure 1.7: Comparison of crystal structures of single metal halide perovskite with chemical formula ABX_3 to metal halide double perovskite with chemical formula $ABB'X_6$. Comparison is specifically made between $CsPbBr_3$ and $Cs_2NaYbCl_6$ (ICSD 50362).

The B-site cation of single MHPs is generally divalent and of a certain size, and of the potential candidates which fill these criteria, lead has by far been the most successful. However, this poses environmental risks upon their degradation to PbX_2, and DPs are a fine candidate for circumventing this problem. As the B-site cations in DPs do not necessarily need to both be divalent, but rather can be mono- and trivalent, the door is opened to many different cations being used instead of lead, rendering DPs an effective approach to developing lead-free MHPs.

1.4.1 The History of Elpasolites

Much like perovskites themselves, DPs have seen an explosion of interest in the last decade despite being known since the discovery of K_2NaAlF_6, elpasolite, in 1883.[75-76] As this discovery

predated the discovery of X-ray diffraction, the structure of elpasolite remained a mystery until 1932.[77] The first reported synthesis of a DP, $Cs_2Au^IAu^{III}Cl_6$, was performed in 1922, with its crystal structure being determined in 1938.[78-79] Further DP research until the 1970s was mainly focused on discovery and structural analysis of new materials, many of which contained lanthanides.[80-82] This investigation shifted towards the electronic and magnetic properties of these lanthanide-containing DPs,[83-85] as well as the generation of luminescent materials *via* doping of lanthanides and transition metals.[86-88] This, as well as the study of mixed valency in materials such as $Cs_2BAu^{III}X_6$ (B = Ag^I, Au^I, X = Cl, Br, I)[89-90] dominated DP research until the 21st century when, in 2014, Cs_2SnI_6 was reported for use as a hole transport material (HTM) in a photovoltaic device.[91] Though this material was not reported as being a DP, it spurred computational studies investigating the potential of DPs as inherently photoactive materials.[92-94] This culminated in the reported synthesis of Cs_2AgBiX_6 (X = Cl and/or Br) in 2016 by three independent groups,[38, 95-96] which has since caused a cascade of research into different DPs for various applications such as upconversion, X-ray detection, photovoltaic devices and photocatalysis.[97-100] Recently, DP research has taken the form of double perovskite nanocrystal (DP NC) synthesis,[101-103] as NCs often have simple and effective synthetic procedures and result in solution processable particles. They can also take advantage of quantum effects at the nanoscale size regime to further tune the properties of the material.

1.4.2 Electronic Structure: Single Perovskite vs. Double Perovskite

As previously discussed (Section 1.3.4), the electronic structure of single perovskites is primarily determined based on the nature of the BX_6 octahedron network. As such, there is little variety present in the lead halide perovskites ($CsPbX_3$, $MAPbX_3$, $FAPbX_3$) as they all share the same B-site cation. The A-site cation can play a role in distorting the octahedral network, thus

affecting the electronic structure, and which halide (or mixture of halides) is present will of course affect the structure by changing the nature of the BX_6 octahedra. However, this all results in a limited variety of electronic structures possible. Being composed of two B-site cations of different valence, DPs contain two different BX_6 octahedra in their crystal structure, and their electronic structure is a result of the combination of both those octahedra.[104] As the B-site cations can also be much more varied in DPs as opposed to single perovskites, this results in a myriad of possible electronic structures. The band-edge optical absorption of single MHPs is a transition from the halide *p*-orbital to the Pb *p*-orbital and can be considered as a ligand-to-metal charge transfer (LMCT), and often results in a direct band gap.[105-106] The same cannot be said for DPs as the band-edge transition is often a metal-to-metal charge transfer (MMCT),[104] and thus relies on the highest occupied molecular orbital (HOMO) and lowest unoccupied molecular orbital (LUMO) of the BX_6 and $B'X_6$ octahedra. Selection of the B and B' cations can, therefore, result in a small, large, direct, or indirect bandgap, making DPs a much more flexible material as their electronic structure can be much more freely modified than single perovskites.[107] However, this causes some of the main weaknesses of DPs as well, namely their often-low quantum yields resulting from indirect bandgaps.[108-111] This, however, can be mitigated by alloying or doping, which both involve the inclusion of foreign atoms. Alloying includes a stoichiometric amount of impurity, as in $Cs_2Ag(Bi_{1-x}Tl_x)Br_6$,[112-113] which can change the electronic structure of the material as in Figure 1.8. As Bi^{3+} is replaced by Tl^{3+}, the Bi 6s character decreases and the Tl 6s character increases, causing the bandgap to change from indirect to direct. In the instance of doping, a small amount of impurity, on the order of 1-2 atom% or less, is included in the crystal structure which can introduce new energy states and potentially improve the material's electronic properties.[114-115]

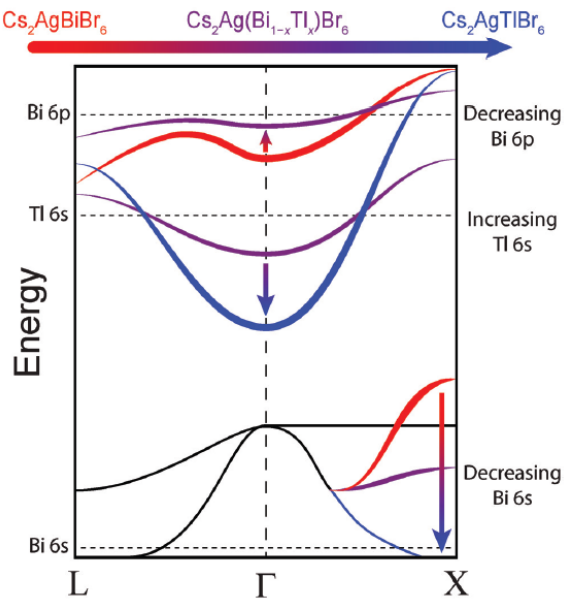

Figure 1.8: Schematic band diagram showing the change in electronic structure over the composition range of the $Cs_2Ag(Bi_{1-x}Tl_x)Br_6$ solid solution. The bands or portions of bands that change upon alloying are colored. The red and blue lines correspond to the bands of $Cs_2AgBiBr_6$ and $Cs_2AgTlBr_6$, respectively, while purple shows an intermediate composition. Horizontal dashed black lines show the approximate energies of the isolated molecular orbitals (reprinted with permission from ref. 113)

1.5 Goals and Scope

The proceeding chapters will discuss the synthesis of MHPs in novel forms. Chapter 2 will discuss the electrochemical deposition of $CaCO_3$ microstructures and their subsequent conversion *via* ion-exchange reactions to $CsPbBr_3$. Focus is placed on the exact nature of the final product and the mechanism though which it is formed. Chapter 3 details the synthesis of $Cs_2NaYbCl_6$ nanocrystals *via* hot injection method. Despite being a known material, $Cs_2NaYbCl_6$ has yet to be reported as being synthesized in nanocrystal form, and its properties as a photoactive material are herein explored.

Chapter 2: Conversion of Electrochemically Deposited Aragonite Crystallites to Perovskite through In Situ Ion Exchange

Metal-halide perovskites (MHPs) are a class of crystalline materials typically adopting a cubic or orthorhombic crystal system and a chemical formula ABX_3 (A, B = cations, X = halide) where the A cation resides in a hole formed from eight corner-sharing BX_6 octahedra. They have garnered much interest in the field of solar energy conversion due to their unique optoelectronic properties, including low exciton binding energy, long charge carrier diffusion distances, and tunable band gaps.[116-118] These properties make them candidates for many light-based processes and devices, including as catalysts in chemical transformations (not limited to solar fuels generation),[119] and as active layers in photovoltaics, light-emitting diodes, and radiation detectors.[120-126] It is now well established that the optoelectronic properties of MHPs are strongly dependent on their structural and morphological dimensionality. Many of these properties are crucial to the design and implementation of solar energy conversion architectures (*e.g.*, active layers in photovoltaics) and include variations in directional transport of charge carriers, reduction of exciton recombination, and decreasing the number of trap states.[127] Recently, a wide range of MHP nanocrystal (NC) morphologies have been reported (nanowires, nanorods, nanosheets, etc.) and these typically exhibit bulk (3D) or quantum-confined (2D or 0D) properties. Developing synthetic methods to preferentially prepare specific morphologies remains an important avenue of research and coupling the properties of ensembles of the nanomaterials in microscale architectures is of additional interest (as evidenced in recent reports of MHP NC superlattices).[128]

Hybrid organic-inorganic perovskites (where the A-site cation is organic) are of great interest for their superior optoelectronic properties. Their use in photovoltaic devices has been pivotal in pushing the efficiencies of these devices to unprecedented levels, competitive with those observed in commercial crystalline silicon devices,[129] but one of their main challenges is reflected in their poor stability (particularly with respect to heat and ambient humidity).[55-57] All-inorganic perovskites (where the A-site cation is inorganic), such as those based on cesium, lead, and halide ions, however, are expected to be more stable (presumably due to the elimination of comparatively weakly bonded organic ions) while still being a versatile and tunable material, thus making them of great interest for solar energy conversion.[55-56, 130] Many procedures exist for direct synthesis of different perovskite active layers for solar energy conversion,[123, 131-132] but often these methods limit the degree of control over the morphologies that can be prepared.[133] Target morphologies are dictated by the desired application of the material; high quality crystalline layers with fused grain boundaries for light-emitting or solar electricity applications *versus* shape and preferentially oriented, high surface area crystallites or particles for photocatalysis applications.[119]

Calcium carbonate is a material that is found with varied morphology in nature, and most typically as the thermodynamically stable calcite or aragonite and metastable vaterite polymorphs. Many of these, and modifications of their arrangements, are accessible *via* bioinspired (biomineralization) syntheses.[134] One such method is electrochemical deposition, where an applied bias initiates $CaCO_3$ deposition at a working electrode.[12] This method affords control over morphology and chirality through additives in the deposition solution, and typically results in the generation of nano- to microstructures on the electrode surface.[12] In this process, a potential is applied across an aqueous solution of sodium bicarbonate and a calcium feedstock such that electrons flow from the cathode into the solution and partially split water into H_2 and OH^- ions.[12]

The resulting hydroxide ions can then deprotonate bicarbonate to yield water, leaving the resulting carbonate to react with calcium cations to produce calcium carbonate. If additives are present in the deposition solution, they may be incorporated into the crystal lattice as the deposition proceeds; as they do, they can inhibit or promote the growth of certain crystal facets, thus causing different morphologies to form. The nature of the final structure is dependent on the identity and action of the additives themselves, where the addition of magnesium cations has previously been found to yield rosette aragonite structures while organic acids yield "barrel-like" structures.[12, 135] This former behavior is based on the known relationship between the Mg/Ca ratio and temperature on calcium carbonate precipitation in sea water.[136]

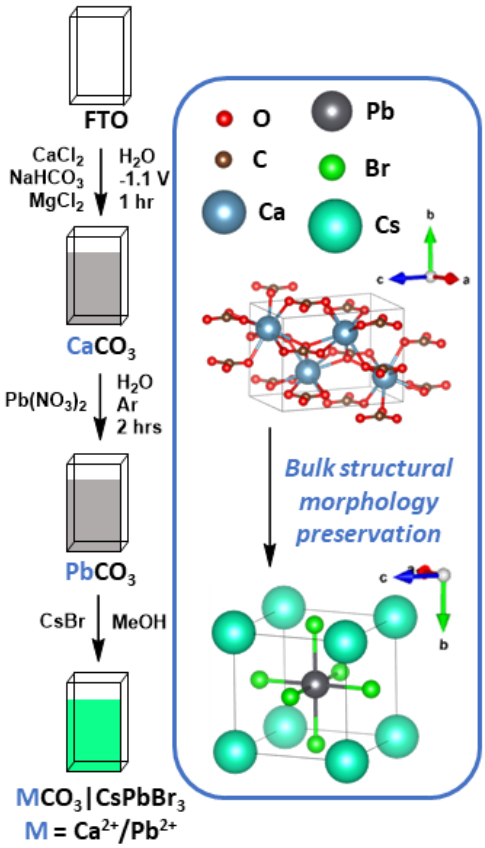

Scheme 2.1. Electrochemical deposition and ion-exchange conversion protocol for the calcium carbonates described in this work.

The conversion of carbonates to hybrid organic-inorganic perovskites with retention of crystal structure has been previously reported using *in situ* ion-exchange reactions to convert barium, strontium, and calcium carbonates to methylammonium lead halide perovskite on a SiO_2 scaffold.[133] The present work aims to synthesize all-inorganic cesium lead halide ($CsPbX_3$, X = Br, Cl, I) perovskite through electrochemical deposition of aragonite calcium carbonate $CaCO_3$ microstructures and subsequent conversion *via* ion-exchange (to $PbCO_3$ and finally the target MHP) with retention of hitherto inaccessible microstructure crystal morphology (Scheme 1).

2.1 Experimental

2.1.1 Materials

Reagents for the electrochemical deposition and conversion of calcium carbonate, sodium bicarbonate ($NaHCO_3$, ACP Chemicals Inc.), calcium chloride dihydrate ($CaCl_2 \cdot 2H_2O$, Fisher), lead nitrate [$Pb(NO_3)_2$, Fisher], cesium bromide (CsBr, Alfa Aesar), magnesium chloride ($MgCl_2$, Alfa Aesar), methanol (99.8%, ACP) were used as received. The working electrode substrate used for deposition, fluorine-doped tin oxide (FTO) coated glass (Sigma-Aldrich), was cleaned through sequential three-fold sonication in soap solution (Sparkleen laboratory detergent for manual washing, Fisher), distilled water, and acetone (99.5%, Fisher) prior to use.

2.1.2 General Methods

All characterization methods, unless otherwise specified, were performed with the sample kept on the original FTO substrate on which it was deposited and/or converted. The microstructures on FTO were first imaged with optical microscopy using a Leitz Laborlux 11 Pol S microscope with a color Axiocam 105. Powder X-ray diffraction (PXRD) patterns were obtained using a Bruker

D8 Advance (Bruker AXS, Madison, WI, USA) equipped with Cu*K*α X-ray source (wavelength, λ = 1.54 Å, radiation operating at 40 kV and 40 mA), a LYNXEYE linear position sensitive detector (Bruker AXS, Madison, WI) and a nickel filter. Data was collected using a continuous coupled θ/2θ scan in the 2θ-range of 20-60 ° with an integration time of 0.2 seconds and step size of 0.02 °. Samples were analyzed by placing the sample slide on a zero-background silicon wafer and being manually brought to the scanning height with a raised platform. This arrangement prevented the rotation of the sample. Scanning electron microscopy (SEM) and elemental analysis by energy dispersive X-ray spectroscopy (EDS) were performed on an SEM FEG JSM-7600TFE field-emission scanning electron microscope (JEOL), with X-Max 80 SDD EDS detector (Oxford). Micrographs were obtained with an acceleration voltage of 5-10 keV, and elemental analysis was carried out with an acceleration voltage of 15 keV. Solid state emission was measured using a PTI QuantaMaster 8075 spectrofluorometer (Horiba) equipped with a 75 W Xe lamp shining through a Czerny-Turner monochromator (λ_{ex} = 365 nm) and a slide holder accessory positioned at 120 °. Samples were scanned with a step size of 1 nm and an integration time of 1 second. Diffuse reflectance spectroscopy (DRS) was performed using a Cary6000i spectrophotometer (Agilent) equipped with an integrating sphere. Fluorescence microscopy images and supporting videos were captured at 60× magnification on a Nikon Ti microscope equipped with a 60× (NA1.45) lens, and Photometrics Prime BSI camera; crystallites were illuminated with a 488 nm laser, and an appropriate filter cube (excitation: 488/10 nm, emission: 500-575 nm). Due to the high NA of the 60× lens, samples were required to be suspended in LDF Oil (R.I 1.515, 700 cSt viscosity), and covered by a #1.5 coverslip. Inductively coupled plasma mass spectrometry (ICP-MS) analysis was done using an Agilent 7500ce (Agilent). Br, Ca, Cs and Pb standards were mixed and diluted with 0.06% HCl. The calibration curves were established

using the standard solutions at concentrations of 0, 0.05, 0.1, 1, and 10 ppm. Samples were run as individual batches after having been digested in 0.06% HCl. High resolution transmission electron microscopy (HR-TEM) was done using a Talos L120C TEM (Fisher) in bright field, with an accelerating voltage of 120 kV. Samples were scraped off their FTO substrate with a razor blade, suspended in hexanes, and sonicated for 10 minutes before being deposited on 300 mesh Au TEM grids with ultrathin carbon film on lacey carbon support film (Ted Pella). Auger electron spectroscopy was performed using a JEOL JAMP-30 Auger scanning electron microscope with an accelerating voltage of 3-10 keV. Diffuse reflectance infrared Fourier transform spectroscopy (DRIFTS) spectra were collected using a Nicolet 6700 FTIR with diffuse reflectance Smart Collector accessory (Fisher).

2.1.3 General Deposition Procedure

The electrochemical deposition of calcium carbonate was performed by first preparing a 100 mL aqueous reaction mixture in a 100 mL volumetric flask containing 59.6 mg of $NaHCO_3$ (7.10 mM), 60.3 mg of $CaCl_2 \cdot 2H_2O$ (4.10 mM), and 61.2 mg of $MgCl_2$ (6.40 mM, for a general reaction scheme see Appendix Figure A1). The reaction mixture was loaded into a 100 mL beaker, and argon was bubbled through the solution for 1 hour, after which the solution was heated to 45 °C. Once this temperature was reached, bulk electrolysis was performed using a bipotentiostat (WaveDriver 20, Pine Research Instrumentation Inc.) with an applied potential of −1.1 V (vs. Ag/AgCl), with a platinum wire counter electrode and FTO working electrode, for 1 hour. Upon completion, the deposited film on FTO was rinsed with distilled water and left to air dry.

2.1.4 General Conversion Procedure

This conversion was performed in two separate steps. The first involved the conversion of the $CaCO_3$ to $PbCO_3$, followed by the second step where $PbCO_3$ from the first step was exposed to a solution of CsBr. The conversion of electrochemically deposited $CaCO_3$ to $PbCO_3$ was performed by first preparing an aqueous solution of $Pb(NO_3)_2$ (25 mL, 3.0 mM). This solution was transferred to a plastic 50 mL centrifuge tube and was sparged with argon for 1 hour, followed by insertion of the $CaCO_3$ FTO film under an Ar atmosphere. The FTO was left in the solution for 2 hours, after which it was removed, rinsed with distilled water, and left to airdry. The second step of the conversion process to transform $PbCO_3$ to perovskite was carried out by first preparing a solution of CsBr (50 mL, 7.09 mM) in methanol. The $PbCO_3$ FTO was held in the solution by forceps for 30 seconds with stirring. At the end of the conversion period, the FTO was removed from the solution, rinsed with methanol, and left to air dry. The resulting FTO was kept in a desiccator (over $CaSO_4$) to preserve the quality of the perovskite material.

2.1.5 Synthesis of OLAM-X

OLAM-Cl was synthesized by first adding 100 mL ethanol 99 % and OLAM (70 %, 18.0 mL, 38.0 mmol) to a round-bottom flask with a magnetic stir bar. The solution was placed in an ice bath with vigorous stirring (~1000 rpm) and put under N_2 inert atmosphere. HCl (12 M, 6.30 mL, 76.0 mmol) was slowly added to the reaction solution and the solution was left stirring overnight. Once complete, the product was isolated by rotary evaporation, leaving behind a gum-like substance. The product was washed with minimal amounts of diethyl ether and vacuum filtered. The resulting waxy white product was dried in a vacuum oven at 80 °C overnight before further use. Synthesis of OLAM-I was performed by adding I_2 (12.94 mg, 1.700 mmol) and OLAM (70 %, 2.55 mL,

5.43 mmol) to a scintillation vial with a magnetic stir bar. The solution was left stirring overnight, resulting in a thick, dark-coloured paste which was used as-is for ion exchange reactions.

2.1.6 General Anion-exchange Procedure

For the anion-exchange of $CsPbBr_3$ to $CsPbCl_3$ or $CsPbI_3$, OLAM-Cl (40.0 mg) or OLAM-I (200.0 mg) were added to a scintillation vial and dissolved in 10 mL of toluene, respectively. The $CsPbBr_3$ sample to be converted was deposited in the vial making sure the face containing the microstructures was not face-down at the bottom of the vial. The reaction vessel was placed on an orbital shaker plate for 1 minute or 1 hour. Once the time had elapsed, the sample slide was removed from the conversion solution with tweezers, rinsed with toluene, and left to air-dry before being stored in a clean scintillation vial and characterized.

2.2 Results & Discussion

Electrochemical deposition of $CaCO_3$ using a modified literature procedure[12] from an aqueous solution of $NaHCO_3$ (7.10 mM), $CaCl_2 \cdot 2H_2O$ (4.10 mM), and $MgCl_2$ (6.40 mM) at 45 °C results in dendritic microstructures of $CaCO_3$ (as observed by light optical microscopy, Figure 2.1A). Microstructures were deposited for 1, 5, 10, 30, and 60 minutes and exhibit different morphologies between each stage of crystallite growth *via* optical microscopy (Figure A2). Powder X-ray diffraction (PXRD) patterns were recorded for each of these growth stages and it was observed that the crystallites deposited appear amorphous at low deposition times, gradually growing and more closely resembling the expected aragonite structure with prolonged deposition time (Figure A2).[137-138] Samples produced by 60 minute deposition were deemed the most suitable for further reaction as they most resembled aragonite as determined by PXRD.

Upon exposure to an aqueous $Pb(NO_3)_2$ solution, optical microscopy shows that the microstructures retain their morphology but appear less visibly transparent (Figure 2.1B), and, once converted in the final conversion step to $CsPbBr_3$ by exposure to a solution of CsBr in methanol, show no discernable change in appearance, once again retaining microstructure morphology (Figure 2.1C). Scanning electron microscopy (SEM) shows that the $CaCO_3$ microstructures are deposited with sizes on the order of 10-50 μm in length (Figure 2.1D). On conversion to $PbCO_3$, SEM shows that, while the microstructure morphology is maintained, the microstructures gain a textured surface (Figure 2.1E). The microstructure surface initially appears as a smooth collection of fused rods or needles prior to exposure to the lead solution (Figure 2.1D), whereas on conversion, qualitatively, it appears as though most visible surfaces have fissured (Figure 2.1E). We anticipate that this change in surface texture is the result of the formation of cerussite in the interface-mediated dissolution of $CaCO_3$ and precipitation of $PbCO_3$.[139]

A recent study by Kim *et al.* provided insight into this conversion process for all three polymorphs of $CaCO_3$ and found that the mechanism is one of interface-mediated dissolution/recrystallization in acidic solution.[140-142] All three polymorphs showed the capacity to undergo the conversion, but with different efficacies dictated by solubility constant, dissolution rate, crystal habit, and surface areas of the initial microstructures. Vaterite and aragonite, growing in polycrystalline aggregates, possess higher surface area than euhedral single crystal microstructures of calcite, causing faster dissolution on exposure to an acidic solution. This leads to a faster reaction of CO_3^{2-} ions with aqueous Pb^{2+} ions, leading to preferential formation of $PbCO_3$. Vaterite was found to have a larger dissolution rate than aragonite, so that the $CaCO_3$ microstructure would dissolve more quickly than $PbCO_3$ could form, leaving a large void between the two layers. Alternatively, in aragonite, the dissolution rate and rate of $PbCO_3$ precipitation are

equivalent, making it so the void at the interface between the two materials is much smaller, creating a more tightly layered composite. This causes the resulting $PbCO_3$ formed over the initial $CaCO_3$ microstructure to precipitate in much the same morphology as the layer beneath, effectively allowing for the retention of crystal morphology, though causing the change in surface texture and apparent reduction in transparency (Figures 2.1B, E).[140] It is anticipated that this type of cerussite shell may be porous, allowing Pb^{2+} ions in solution to migrate to the $CaCO_3/PbCO_3$ interface to continue the process of conversion to $PbCO_3$.[139, 143] The pH of the $Pb(NO_3)_2$ conversion solution in the present work was measured and was found to be acidic with an average pH of 3.92, hence, we propose that the conversion process proceeds by the same mechanism outlined above.

Upon conversion to the anticipated final perovskite product (Figure 2.1F) the microstructure surface appears to be damaged while maintaining the overall microstructure morphology. This change may be brought about by the same process where the surface of the microstructure partially dissolves (on extraction of Pb^{2+}) and reacts with the ions present in solution to produce a surface layer of $CsPbBr_3$, causing a change in surface texture while retaining overall microstructure morphology.

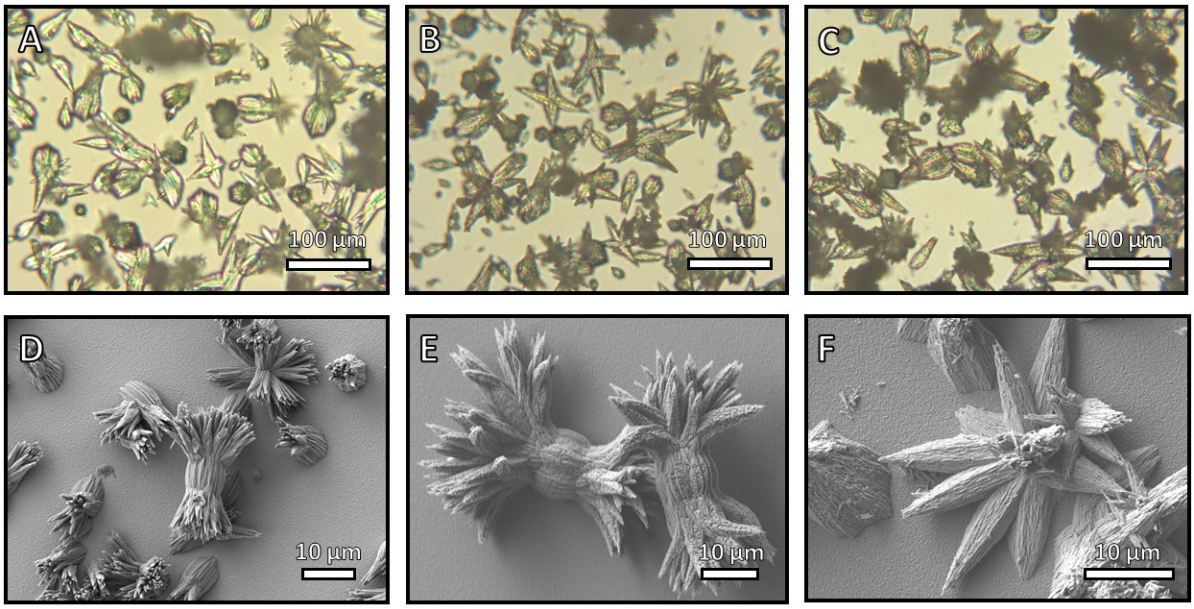

Figure 2.1. Optical micrographs of (A) $CaCO_3$ grown as aragonite, (B) microstructures after conversion to $PbCO_3$, and (C) microstructures after conversion to $CsPbBr_3$ taken at 50× magnification with (D-F) corresponding scanning electron micrographs. All samples were analyzed on the FTO substrate on which they were originally deposited and converted.

PXRD patterns were collected of the substrate fluorine-doped tin oxide (FTO) and the resultant material at each step of the deposition and conversion processes (Figure 2.2A). We note that the reflections at $2\theta = 26.4°$, 33.6°, and 37.6° present in the collected patterns are characteristic of the substrate FTO, as denoted by the black lines aligned with the same reflections in the pattern of the blank substrate FTO. The patterns collected for $CaCO_3$ and $PbCO_3$ resulting from electrochemical deposition and conversion, respectively, match the simulated patterns for their respective naturally occurring orthorhombic polymorphs, aragonite and cerussite. Despite repeated attempts across many samples prepared under varying conditions, the collected pattern of the final conversion product does not match the simulated pattern for cubic perovskite $CsPbBr_3$, but rather that of cerussite. This may indicate that the conversion to $CsPbBr_3$ does not permeate the entire microstructure but rather a thin surface layer.

These findings were confirmed by SEM energy dispersive X-ray spectroscopy (EDS, Figure 2.2B). Spectra were collected after deposition and at each conversion step, and while those of $CaCO_3$ and $PbCO_3$ adhered to expectations, $CsPbBr_3$ did not. The former showed peaks characteristic of Ca and Pb, respectively, along with C and O and atomic percentages close to the expected M:C:O ratio of 1:1:3 (M = Ca or Pb). As for the latter $CsPbBr_3$, while peaks for Pb, Cs, and Br were present, there were also peaks characteristic of C, O, and Ca. The atomic percentages collected also show Cs and Br in much lower amounts than are expected, exhibiting a Cs:Pb:Br ratio of 1:2.8:1.1 rather than the expected 1:1:3 (Table A1). However, SEM-EDS mapping data confirm the presence of Cs and Br in the general confines of the microstructure (Figure A3). Similarly, diffuse reflectance infrared Fourier transform spectroscopy (DRIFTS, Figure A4) confirms the presence of carbonates of both Pb^{2+} and Ca^{2+}. Modes at 712, 850, 1082, 1500, and 1787 cm^{-1} were observed for $CaCO_3$, and these same bands were observed in $PbCO_3$ samples along with a set of slightly shifted corresponding peaks ($\Delta \approx 42$ cm^{-1}), signifying the presence of both $CaCO_3$ and $PbCO_3$ in the $PbCO_3$ microstructures. No modes, or the disappearance of existing modes, attributable to the formation of $CsPbBr_3$ were observed.

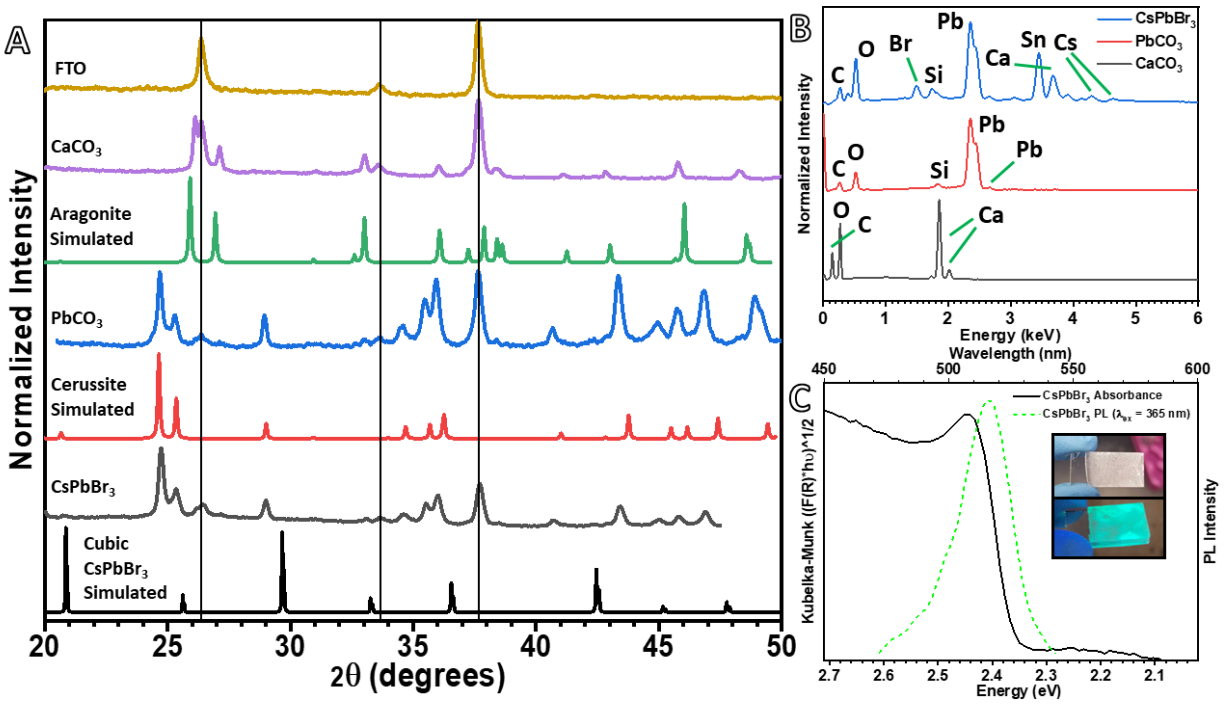

Figure 2.2. (A) Powder X-ray diffraction patterns of samples after deposition and ion exchange reactions with corresponding simulated patterns ($CaCO_3$ ICSD 157993, $PbCO_3$ ICSD 6178, $CsPbBr_3$ ICSD 29073). (B) Energy dispersive X-ray spectra of $CaCO_3$ after deposition, and $PbCO_3$ and $CsPbBr_3$ after respective conversion steps. (C) Diffuse Reflectance UV-Vis and photoluminescence (PL, λ_{ex} = 365 nm) spectra of $CsPbBr_3$ microstructures in the solid state on FTO slides (inset images of sample in visible and λ_{ex} = 365 nm UV light).

These techniques lack surface sensitivity, so Auger electron spectroscopy (AES) was used to analyze the chemical composition of the microstructure surface. Despite a high degree of sample degradation, peaks corresponding to Cs, Br, as well as Pb were observed along with C and O (Figure A5) correlating to our data from SEM-EDS. Analysis of SEM micrographs taken in the secondary electron scanning mode of a broken microstructure reveal a difference in chemical composition between the surface and interior of the microstructures (Figure A6). Spot SEM-EDS analysis of the surface and exposed interior show different chemical compositions where the former correlates to our earlier SEM-EDS findings, while the latter much more closely resembles $CaCO_3$ in composition (Figures 2.2B, A4). Taken together, these results support that each

conversion process does not permeate the microstructures completely, but rather up to an unspecified depth within the microstructure.

The photoluminescence (PL) of the fully converted product was measured in the solid state on the FTO substrate. An emission peak was found to be centered around 517 nm (Figure 2.2C), matching values reported for $CsPbBr_3$ perovskite nanocrystals (PNCs, ca. 500-520 nm, Figure A7)[33, 144-145] rather than matching the emission maximum of $CsPbBr_3$ microstructures (ca. 530-550 nm).[72, 74, 146] The absorbance of this material was measured *via* diffuse reflectance UV-Vis spectroscopy (DRS, Figure 2.2C). An optical bandgap energy of 2.36 eV was determined correlating to values reported for $CsPbBr_3$ PNCs rather than microstructures.[33, 72, 74, 144-146]

Fluorescence microscopy (FM) was employed to visualize the microstructures upon full conversion to determine the extent to which the microstructure surface was converted to perovskite. Figure 2.3A shows that photoluminescence is observed from the entire profile of the microstructures, qualitatively showing that most of the microstructure surface is converted. Different emission intensities were observed between microstructures and within the confines of individual microstructures. A video recording taken during the FM experiment scanning a small area of the sample shows that these regions of different emission intensity on individual microstructures exhibit fluorescence blinking (Supporting Video 1), a phenomenon observed previously in $CsPbBr_3$ PNCs but typically not microstructures.[145, 147-148] Fluorescence blinking is a phenomenon that is attributed to the Auger-ionization of single nanocrystals, whereby electrons are ejected from the particle and subsequent excitons relax non-radiatively to the ground state, leaving the positively charged particle non-emissive until it is neutralized.[149-151] Figure 2.3B is a high-contrast image showing the brightest points of fluorescence blinking on some of the sample microstructures. These points are below the resolution of the instrument (308 nm) and thus in the

nanoscale size regime. These data, taken together with the electron microscopy and PXRD data, suggest that the final conversion step results in a thin surface layer of $CsPbBr_3$ nanocrystals. This nanocrystalline layer may arise because of the dissolution of $PbCO_3$ in the surface facets and subsequent or concomitant rapid formation of $CsPbBr_3$ nanoparticles on the microstructure surface.

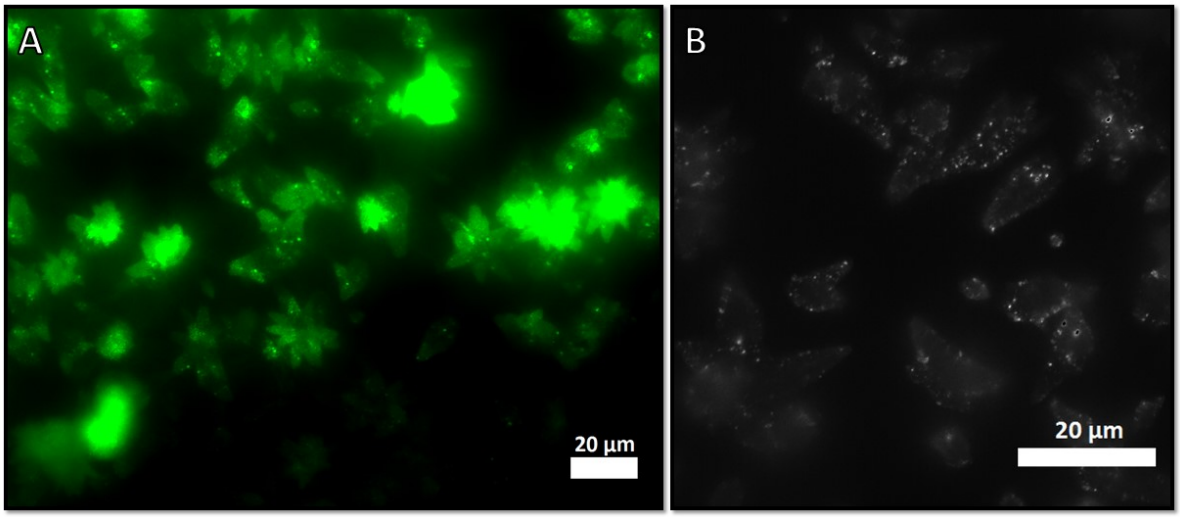

Figure 2.3. (A) Fluorescence microscopy image of crystallites after conversion to $CsPbBr_3$. (B) Photoblinking is observed in areas of higher contrast. (λ_{ex} = 488 nm)

We employed inductively coupled plasma mass spectrometry (ICP-MS) to better determine a chemical composition of the fully converted microstructures (Table A2). On digestion of the surface bound structure in HCl, Br and Cs were found in appreciable amounts in the samples analyzed, and a molar ratio of Cs:Br was calculated for each sample. Of the four samples analyzed (each sample being its own batch), two samples demonstrated a ratio of approximately 2.9, representing the expected stoichiometry of $CsPbBr_3$, while two samples analyzed demonstrated a ratio of approximately 5.8-6.2. This may indicate the presence of different stoichiometries, which can appear in perovskite samples due to the formation of different phases.[34, 152] Furthermore, the final product in this work theoretically does not contain any organic capping groups on the

perovskite surface. In typical $CsPbBr_3$ PNC syntheses, organic surfactants are incorporated onto the nanocrystal surface to passivate it, reduce surface defects, improve colloidal/structural stability, and modulate optoelectronic properties.[64, 67] In this work where as-converted material does not incorporate such a protective layer of capping groups the appearance of different stoichiometries as indicated by ICP-MS is not outside the realm of possibility.

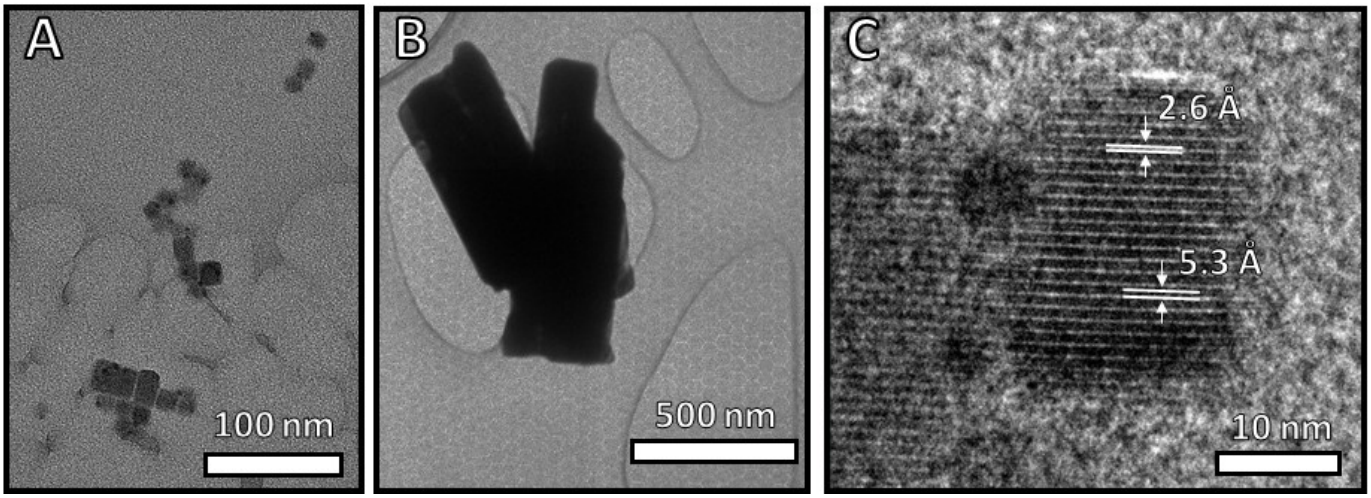

Figure 2.4. Transmission electron micrographs of (A) $CsPbBr_3$ nanoparticles, (B) microstructure fragments, and (C) $CsPbBr_3$ nanoparticle interplanar d-spacing measurements of 2.6 and 5.3 Å for the (210) and (100) crystal planes of cubic $CsPbBr_3$, respectively.

Transmission electron microscopy (TEM) was used to image at an even smaller scale a sample which was scraped off the FTO surface, suspended in hexanes and sonicated (Figures 2.4, A8, A9). The presence of cubic nanocrystals with an average edge length of 14.3 nm was confirmed (Figure 2.4A) resembling those observed from the hot-injection syntheses of $CsPbBr_3$ PNCs previously reported.[33, 67, 147] This further supports the conclusion that the surface of the final product is indeed a thin layer of $CsPbBr_3$ PNCs. Figure 2.4B shows a much larger set of particles, likely broken fragments of the main body of the microstructure composed of $PbCO_3$ and $CaCO_3$. Figures 2.4C shows the crystal planes of one nanocrystal found and the measurement of their

interplanar d-spacing. D-spacing measurements of 2.6 and 5.3 Å were determined, which coincide with the d-spacing of the (210) and (100) crystal planes, respectively, in cubic $CsPbBr_3$.

The same synthetic approach was applied to the direct synthesis of other perovskite halides $CsPbX_3$ (X = Cl, I). Microstructures were electrochemically deposited on FTO, converted to $PbCO_3$, and then exposed to CsCl or CsI in methanol to result in $CsPbCl_3$ or $CsPbI_3$, respectively. The PL spectra of the resulting materials were measured (Figures 2.5A,B).

The directly-synthesized $CsPbCl_3$ exhibits an emission maximum centered around λ_{em} = 405 nm, which is in line with reported values for $CsPbCl_3$ NCs which range from λ_{em} = 400-410 nm.[153-155] For the directly-synthesized $CsPbI_3$, an emission maximum of λ_{em} = 800 nm was measured, and this is significantly red-shifted in comparison to reported values of $CsPbI_3$ NCs which typically range from λ_{em} = 600-700 nm.[156-158] This may be the result of the $CsPbI_3$ nanoparticles being uncapped by any passivating organic groups as is the typical end-product of more traditional synthetic routes. Iodide is the halide with the poorest ability to fit in the cesium lead halide perovskite structure, as indicated by it possessing the lowest Goldschmidt tolerance factor of the three $CsPbX_3$ perovskites,[159] making it particularly susceptible to defects which can potentially alter the electronic structure to such drastic lengths as is seen with the as-synthesized $CsPbI_3$ in the present work. The lack of organic capping groups may also allow the growth of $CsPbI_3$ nanoparticles to sizes larger than those typically reported (ca. 10-20 nm),[156-158] causing a red-shift in emission. It is likely that both phenomena have a role to play in the discrepancy observed in the emission properties given the magnitude of the shift exhibited.

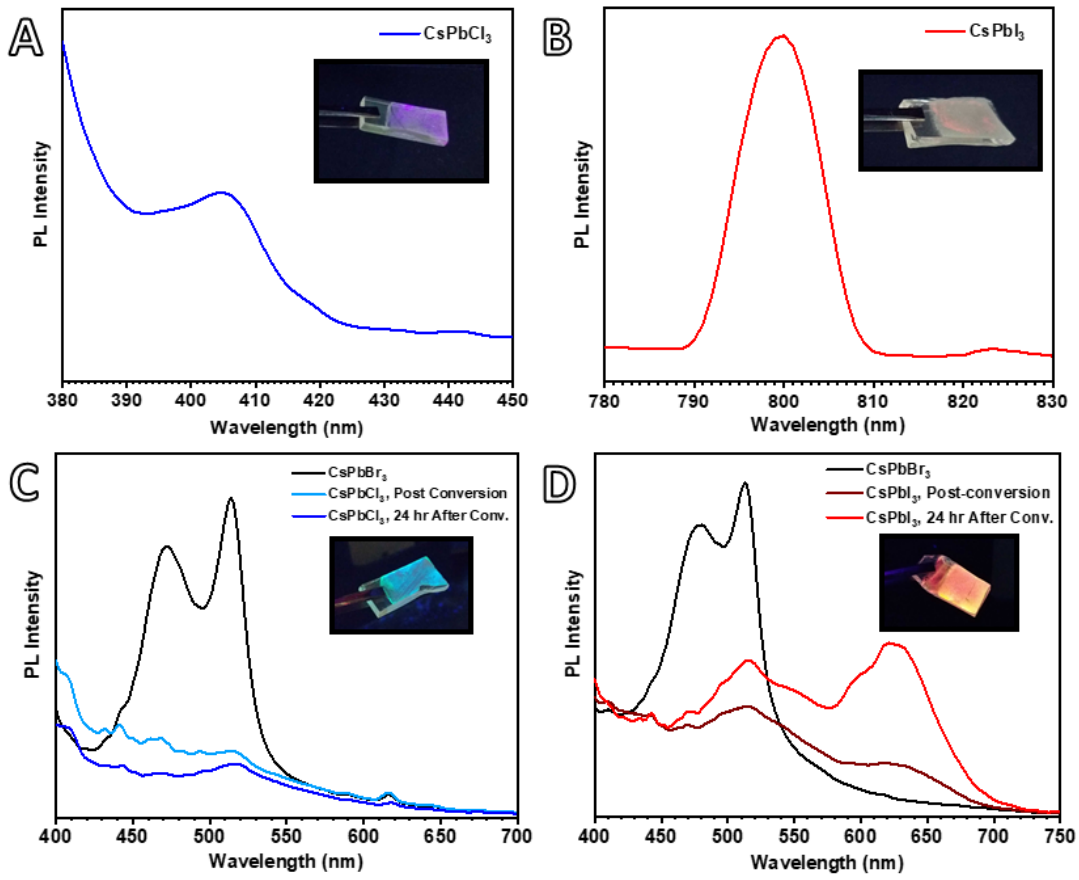

Figure 2.5. PL spectra measured for (A, B) $CsPbCl_3$ and $CsPbI_3$ synthesized directly by the deposition and conversion process adapted for Cl and I, respectively. PL spectra recorded for samples of $CsPbBr_3$ before, immediately after, and 24 hours after being post-synthetically modified *via* anion-exchange to (C) $CsPbCl_3$ and (D) $CsPbI_3$. All spectra were collected with λ_{ex} = 365 nm and contain inset images of the resulting samples under UV lamp irradiation (λ = 365 nm).

The post-synthetic ion-exchange of $CsPbBr_3$ NCs has been reported as a reliable method for altering the composition and electronic properties of MHPs.[68] This procedure was adapted to the present work, and as-synthesized $CsPbBr_3$ samples were exposed to solutions of OLAM-Br and OLAM-I in toluene for 1 minute and 1 hour. The 1-hour samples were no longer emissive, likely due to prolonged exposure of halides which may have deteriorated the PNCs on the microstructure surfaces, or because the PNCs were dislodged from the microstructures and dispersed in the conversion solution. The 1-minute samples, however, did exhibit emission, and their PL spectra

were recorded. The initial emission maximum of $CsPbBr_3$ (λ_{em} = 514 nm) drastically decreases in intensity upon conversion, and a shoulder at λ_{em} = 408 nm is generated (Figure 2.5C). This new emission is a product of the newly formed $CsPbCl_3$, however the fact that characteristic $CsPbBr_3$ emission remains indicates that the conversion was likely not a complete one and, rather, resulted in a mixed halide perovskite $CsPbBr_{3-x}Cl_x$. Similar results are seen with the iodide conversion (Figure 2.5D), where the initial $CsPbBr_3$ emission at λ_{em} = 513 nm dissipates but remains present, while a new peak at λ_{em} = 628 nm is formed, signaling the formation of a mixed halide perovskite, $CsPbBr_{3-x}I_x$, here as well. It should be noted that this emission is much more in line with reported values for $CsPbI_3$ NC emission and may be due to the difference in how the materials are formed by the different procedures. In the post-synthetic exchange method, an existing perovskite crystal lattice already exists and serves as a template when exchanged to the iodide, resulting in a more proper perovskite lattice, albeit a mixed halide one, whereas direct formation of $CsPbI_3$ is difficult owing to its low stability. These results show post-synthetic anion-exchange as a viable route for modulating the electronic properties of materials synthesized by the proposed electrodeposition and conversion method, though further optimization is needed in order to induce complete halide conversion.

2.3 Conclusion

Electrochemically deposited aragonite $CaCO_3$ was successfully converted to the perovskite $CsPbBr_3$ with retention of overall microstructure shape, as evidenced by photoluminescence spectroscopy and fluorescence microscopy. SEM-EDS in the secondary electron scanning mode showed that exposure to a concentrated aqueous solution of $Pb(NO_3)_2$ may trigger a localized dissolution/recrystallization mechanism whereby the microstructure surface is dissolved and

CO_3^{2-} reacts with Pb^{2+} in solution to form a layer of $PbCO_3$. This process is reported as being interface-mediated, causing the resulting microstructure composite to retain the morphology of the original microstructure. Transmission electron microscopy confirms that, upon exposure to CsBr in methanol, the resulting perovskite takes the form of nanoparticles on the surface of the microstructures. Fluorescence microscopy revealed that the as-converted perovskite microstructures exhibit domains of fluorescence blinking, which is a property found in $CsPbBr_3$ PNCs but not microstructures. This work confirms a synthetic pathway for producing the all-inorganic perovskite $CsPbBr_3$ in shapes previously not obtainable. Further work is ongoing to determine if properties (*e.g.*, directing of charge carriers) that might be imparted by the new morphology could prove useful in solar energy conversion and/or photocatalysis applications.

Chapter 3: Synthesis of Novel Double Perovskite $Cs_2NaYbCl_6$ Nanoparticles and Post-synthetic Anion Exchange

Within the last 5 years, perovskites have emerged as a material of great interest in this field as they boast desirable optoelectronic properties such as long charge carrier diffusion lengths, low exciton binding energy, high defect tolerance, high absorptivity, and high quantum yields.[116-118, 160-164] They are a class of semiconductor with the general chemical formula ABX_3 (A = monovalent cation, B = divalent cation, X = anion) and normally occur with a cubic unit cell and belong to the $Pm\bar{3}m$ space group.[34] The most promising composition of these materials is based on lead halides such as methylammonium lead halide ($MAPbX_3$) and cesium lead halide ($CsPbX_3$). Though these materials are standout performers in terms of their optoelectronic properties (particularly with respect to their performance as active layers in photovoltaics), they face stability issues, especially when incorporating organic cations.[55-57] In the presence of moisture and heat, these perovskites tend to degrade, producing PbX_2 as an environmentally hazardous by-product. As such, recent efforts have been focused on creating Pb-free alternatives to the classic lead halide perovskite. Though tin can also exist in the +2 oxidation state, this state is not stable and causes Sn-based perovskites to degrade easily due to oxidation.[165-166]

Elpasolites, or double perovskites, have seen some attention over the years since their first synthesis in 1922, primarily for the sake of identifying and structurally analyzing new compositions in this class of material.[113, 167] In the 1970s, interest in these materials grew particularly with respect to their magnetic properties, but not until recently have they been looked

upon for their optical properties as a potential Pb-free alternative to Pb-containing perovskites in solar energy conversion.[113, 168] Double perovskites resemble perovskites in structure, but they differ in chemical formula. If the chemical formula of a perovskite, ABX_3, is doubled, the resulting chemical formula would be $A_2B_2X_6$, the general formula for a double perovskite. This allows the replacement of Pb^{2+} as the divalent B cation with a monovalent and trivalent cation, B and B', which maintain the electroneutrality of the compound but allow for the creation of Pb-free perovskite materials such as Cs_2AgBiX_6.[38]

Though double perovskites have been studied in the past, these studies focused more on bulk materials.[81] In the recent age of surging interest in nanomaterials, many synthetic methods have been developed to synthesize these materials in the nanoscale size regime as nanoparticles.[101, 109, 169-171] Synthesizing a material as nanoparticles can endow it with application-dependent favourable properties such as enhanced surface area and size dependent optical properties allowing for fine tuning of the material. The present work aims to synthesize $Cs_2NaYbCl_6$ nanoparticles and perform ion exchange reactions post-synthetically to demonstrate the tunability of the material.

3.1 Experimental

3.1.1 Materials

Reagents for the hot injection synthesis of $Cs_2NaYbCl_6$ nanocrystals, sodium acetate (NaAc, $NaC_2H_3O_2$, ACP), ytterbium(III) acetate tetrahydrate ($YbAc_3$, $Yb(C_2H_3O_2)_3{\cdot}4H_2O$, Sigma-Aldrich), oleylamine (OLAM, $C_{18}H_{37}N$, 70%, Sigma-Aldrich), diphenyl ether (DPE, $(C_6H_5)_2O$, Acros), cesium carbonate (Cs_2CO_3, Alfa-Aesar), octadecene (ODE, $C_{18}H_{36}$, 90 %, Alfa-Aesar), and oleic acid (OA, $C_{18}H_{34}O_2$, 90%, Alfa-Aesar) were used as received. Oleylammonium iodide and bromide (OLAM-I, OLAM-Br) were synthesized *via* previously reported procedures using

oleylamine (70%), iodine (I_2, Sigma-Aldrich), hydrobromic acid (HBr, 48%, Sigma-Aldrich), and ethanol (99%, Greenfield).

3.1.2 General Methods

Powder X-ray diffraction (PXRD) patterns were obtained using a Bruker D2 Phaser 2nd Generation PXRD (Bruker AXS, Madison, WI, USA) equipped with Cu*K*α X-ray source (wavelength, λ = 1.54 Å, radiation operating at 30 kV and 10 mA), a Si-strip SSD160-2 detector. Data was collected using a continuous coupled θ/2θ scan in the 2θ-range of 20-60 ° with an integration time of 0.4 seconds and step size of 0.02 °. Scanning electron microscopy (SEM) and elemental analysis by energy dispersive X-ray spectroscopy (EDS) were performed on a Phenom ProX tabletop scanning electron microscope (Thermo Fisher Scientific) with EDS capability. Micrographs were obtained with an acceleration voltage of 5-10 keV, and elemental analysis was carried out with an acceleration voltage of 15 keV. Photoluminescence spectra were measured using a PTI QuantaMaster 8075 spectrofluorometer (Horiba) equipped with a 75 W Xe lamp shining through a Czerny-Turner monochromator (λ_{ex} = 365 nm). Samples were scanned with a step size of 1 nm and an integration time of 1 second. Quantum yields were acquired with the same spectrofluorometer with an integrating sphere equipped. High resolution transmission electron microscopy (HR-TEM) was done using a Talos L120C TEM (Fisher) in bright field, with an accelerating voltage of 120 kV. Samples were suspended in hexanes and sonicated for 10 minutes before being deposited on 300 mesh copper grids with formvar stabilized with carbon.

3.1.3 Synthesis of Cesium Oleate

$CsCO_3$ (203.0 mg, 0.6230 mmol), octadecene (10 mL), and oleic acid (1.00 mL, 3.69 mmol) were added to a 2-neck round bottom flask with magnetic stir bar. The mixture was heated to 150 °C

under N_2 atmosphere with stirring until all solids had dissolved, signalling completion of the reaction. The resulting Cs-oleate was stored in a scintillation vial for future use.

3.1.4 Synthesis of $Cs_2NaYbCl_6$ Nanocrystals

$YbAc_3$ (105.6 mg, 0.2500 mmol) and NaAc (19.7 mg, 0.240 mmol) were added to a 25 mL two-neck round bottom flask. The openings were plugged by septa and the flask was connected to a Schlenk line and put under continuous vacuum for 5 minutes. Afterwards, OLAM (0.500 mL, 1.06 mmol), Cs-oleate (1 mL), and DPE (4 mL, 25.4 mmol) were added to the reaction flask with a magnetic stir bar. With low stirring (~200 rpm), the vessel was placed back under vacuum and heated to 40 °C. Once the temperature was reached, stirring was increased to high stir (~1000 rpm) and the solution was left to dry for 30 minutes. After the time had elapsed, the reaction vessel was flushed with N_2 and slowly brought up to 105 °C. While the solution was being heated, a separate solution of benzoyl chloride (200 μL, 1.72 mmol) and DPE (500 μL, 3.17 mmol) was prepared in a scintillation vial. The vial was sealed with a septum and the solution was sparged with N_2 gas for 5 minutes. Once the reaction solution had reached the target temperature, the benzoyl chloride solution was injected and the mixture was left to react for 5 seconds to 10 minutes after which the reaction vessel was plunged into an ice bath. Once the vessel was cooled to room temperature, the solution was centrifuged at 2377 RCF for 10 minutes, the supernatant was decanted, and the isolated NCs were redispersed in toluene.

3.1.5 Synthesis of OLAM-X

OLAM-Br was synthesized by first adding 100 mL ethanol 99 % and OLAM (14.28 mL, 30.39 mmol) to a round-bottom flask with a magnetic stir bar. The solution was placed in an ice bath

with vigorous stirring (~1000 rpm) and put under N_2 inert atmosphere. HBr (48%, 8.56 mL) was slowly added to the reaction solution and the solution was left stirring overnight. Once complete, the product was isolated by rotary evaporation, leaving behind a gum-like substance. The product was washed with minimal amounts of diethyl ether and vacuum filtered. The resulting waxy white product was dried in a vacuum oven at 80 °C overnight before further use. Synthesis of OLAM-I was performed by adding I_2 (12.94 mg, 1.700 mmol) and OLAM (2.55 mL, 5.43 mmol) to a scintillation vial with a magnetic stir bar. The solution was left stirring overnight, resulting in a thick, dark-coloured paste which was used as-is for ion exchange reactions.

3.1.6 Ion-exchange Reaction with OLAM-X

50 mg of OLAM-Br or 200 mg of OLAM-I (both representing an excess amount) were dissolved in 5 mL of toluene. NCs in toluene (1 mL) were added to the OLAM-X solution and stirred on an orbital shaker plate for 30 minutes. Further characterization was performed on the NCs in solution without extraction.

3.2 Results & Discussion

To our knowledge, reported syntheses of $Cs_2NaYbCl_6$ have only resulted in the formation of bulk double perovskite (DP).[99, 172-174] The reported synthesis of $Cs_2AgInCl_6$ DP NCs[101] was adapted for the first synthesis of $Cs_2NaYbCl_6$ DP NCs. This synthesis resulted in nanoparticles that were primarily spherical in shape with an average size of 12.82 ± 1.914 nm but accompanied by a less common hexahedron morphology with an average size of 25.28 ± 5.275 nm (Figure 3.1A). It has been reported that perovskite NCs produced by hot injection see the majority of their growth in the first few seconds after introduction of the halide precursor.[33] However, this was tested in the present work by extending the reaction time to 1, 5, and 10 minutes after injection of

the halide precursor. The resulting nanoparticles were imaged *via* TEM (Figure 3.1), which shows that the 1-minute reaction time synthesis resulted in NCs that were either spherical or cubic in morphology with average sizes of 10.52 ± 1.219 nm and 11.23 ± 2.16 nm, respectively (Figure 3.1B), similarly to those of the 5-second reaction. However, the cubic nanoparticles present in the 1-minute sample have more defined vertices whereas those in the 5-second sample are truncated cubes, or hexahedra. The 5-minute reaction time synthesis showed similar results in that spherical and hexahedral NCs were observed, however the hexahedra were considerably larger and were accompanied by particles of irregular shape (Figure 3.1C). These larger particles had an average width of 46.79 ± 10.72 nm while the smaller particles exhibit an average size of 14.61 ± 4.48 nm. Finally, the NCs resulting from the 10-minute synthesis were also composed of hexahedra and spheres with average sizes of 25.93 ± 10.90 nm and 18.86 ± 4.356 nm, respectively (Figure 3.1D). These results demonstrate that particle size indeed does not increase dramatically with increased reaction time. However, the phases of the material did vary upon increasing the reaction time, and this was further investigated *via* structural analysis.

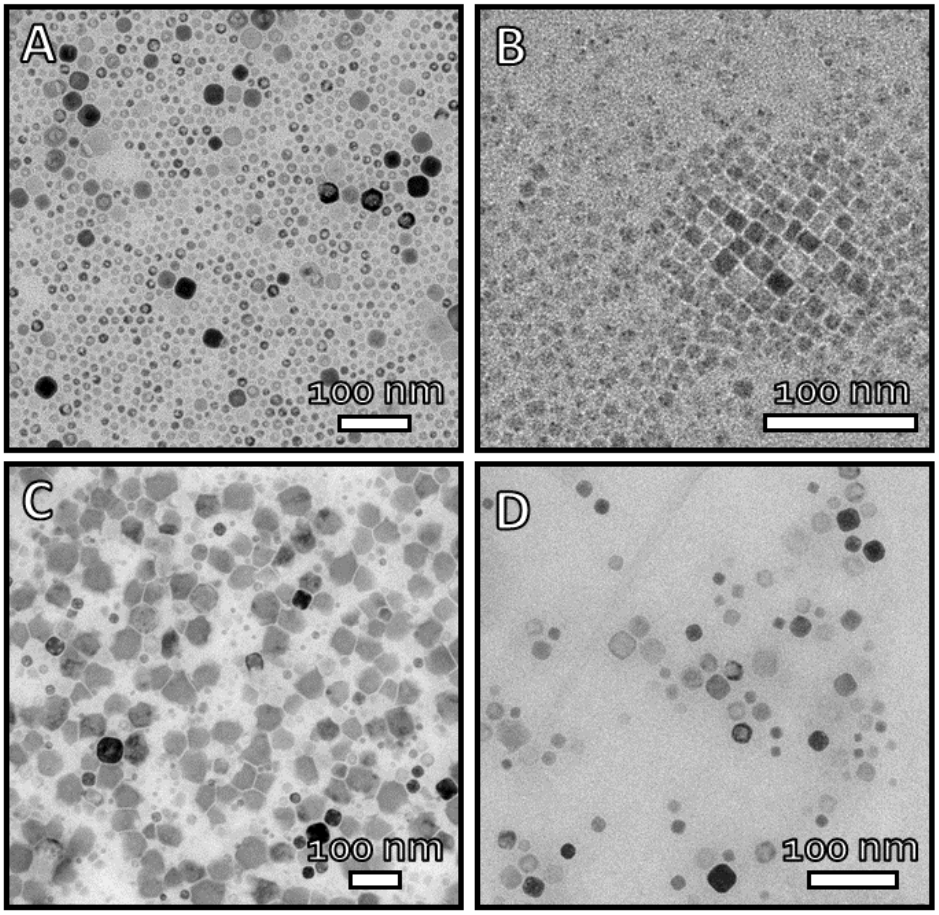

Figure 3.1: Transmission electron micrographs of $Cs_2NaYbCl_6$ nanoparticles produced *via* hot-injection method with a (A) 5 second, (B) 1 minute, (C) 5 minute, and (D) 10 minute reaction time.

Powder X-ray diffraction (PXRD) was employed for the structural analysis of the synthesized NCs (Figure 3.2). In general, the patterns measured for all samples are poorly resolved due to the nature of NC samples in PXRD. The fact the sample is composed of such small particles makes it so that the diffraction observed is not very strong as each individual particle has less material present to diffract the incoming X-rays, causing a worse signal-to-noise ratio. Additionally, as is seen in the particle size discussed earlier for the different samples, there is a large degree of variation in NC size, as the sample is composed of a great number of particles compared to a bulk sample of equal mass, which would have larger particles that are fewer in

number. This causes the broadening of reflections, as is observed in the collected patterns. Despite these conditions, information can be extracted from the observed powder patterns. Debye-Scherrer analysis of each sample's pattern yielded particle sizes which correlate well to those measured *via* TEM. The 5-second sample bears few reflections which match the simulated pattern for bulk cubic $Cs_2NaYbCl_6$, and this matches what was seen *via* TEM where the nanoparticles were primarily composed of spheres. The pattern measured for the 1-minute sample exhibits the sharpest reflections, suggesting the best size distribution of the samples, which coincides with what was seen by TEM as the sample had the smallest deviation of its average particle size. Furthermore, the 1-minute sample pattern contains reflections which coincide with each of the reflections in the simulated pattern, along with a handful of reflections which do not, suggesting the presence of two phases: one cubic and one other (highlighted in Figure A10). This, again, matches the TEM results which showed a set of cubic NCs, which were by far the most well-defined cubic NCs among the different samples, alongside the presence of spherical ones. The 5- and 10-minute samples both show much broader reflections owing to their larger size dispersity, but also show reflections matching those of the simulated pattern. Of particular interest is the lack of reflections arising from a secondary phase. Such reflections can still be identified in both samples' patterns but are noticeably lower in intensity. This is observed in the transmission electron micrographs as well, where spherical NCs are few and far between compared to the larger cubic NCs. The identity of the large irregularly shaped NCs present in the 5-minute sample is, however, an unknown. It is most likely amorphous material contributing to the severe angle at which the two patterns begin from $2\theta = 20\text{-}30\ ^\circ$. A large amount of amorphous material was also present in the 10-minute sample as observed by TEM (Figure A10D). Overall, these data show that carefully increased reaction time may be one viable avenue to obtaining better phase purity for these samples in addition to

other previously explored methods of improving NC polydispersity such as temperature control and centrifugation.

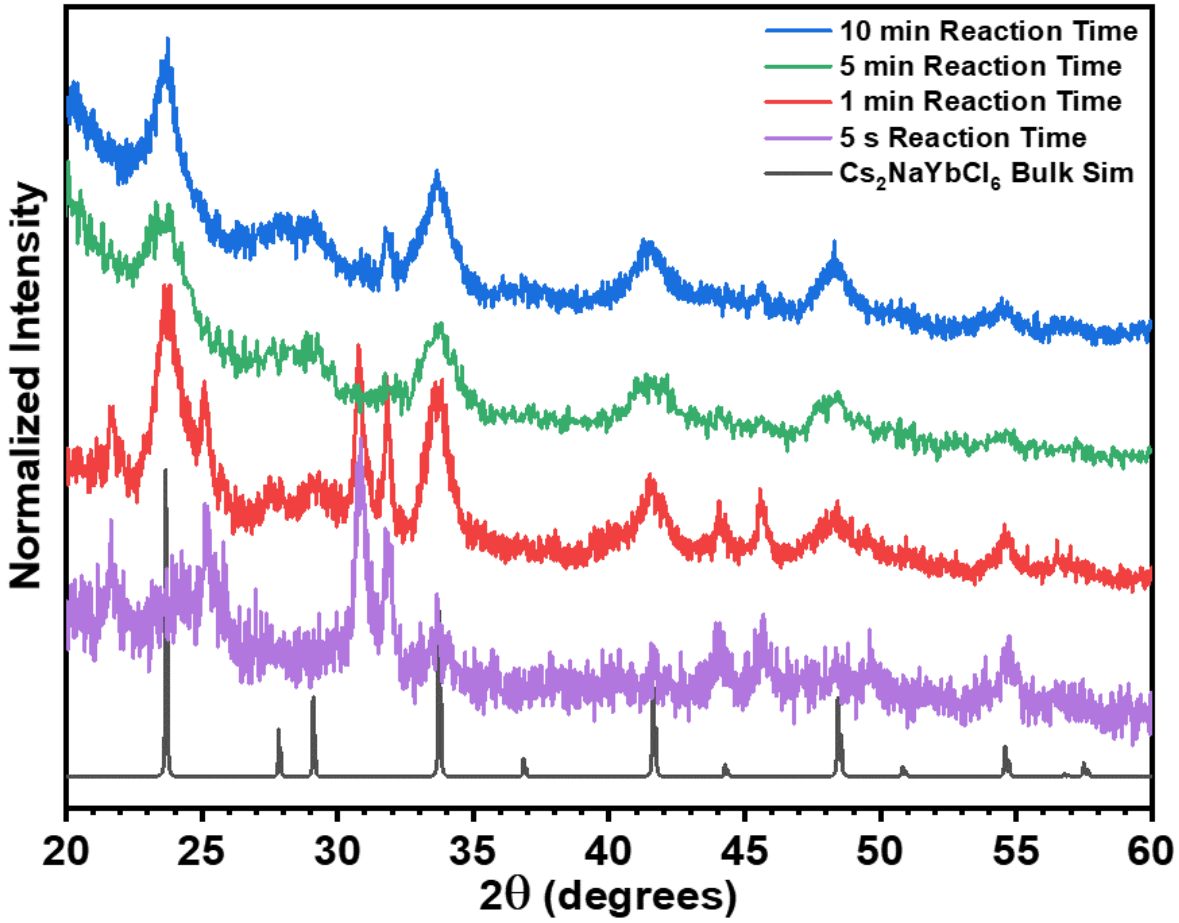

Figure 3.2: Powder X-ray diffraction patterns measured for $Cs_2NaYbCl_6$ nanoparticles produced *via* hot-injection method with a 5 second, 1-, 5-, and 10-minute reaction time as compared to the simulated pattern of bulk cubic $Cs_2NaYbCl_6$ (ICSD 50362).

Chemical composition analysis of the NCs was performed using SEM-EDS. Table 3.1 shows data collected for a 10-minute reaction sample, containing a high atomic percentage of carbon due to the carbon tape upon which the sample was deposited for analysis, and some oxygen which is often present as a native layer on either the sample stage or the sample film itself. If these atomic percentages are not taken into account, one is left with the relative atomic percentages present for Cs, Na, Yb, and Cl that match well with their expected atomic percentages. However,

reproducibility of these findings is challenging with other samples producing atomic percentages which differed from these results, owing to sample vulnerability to beam damage during analysis. As such, these results are taken as a qualitative analysis rather than quantitative, demonstrating the presence of the expected ions.

Element	Atomic %	Relative Atomic %	Expected Atomic %
C	**76.69**	**-**	**0**
O	**2.46**	**-**	**0**
Cl	**11.92**	**57.17**	**60**
Yb	**3.42**	**16.40**	**10**
Na	**2.40**	**11.51**	**10**
Cs	**3.11**	**14.91**	**20**

Table 3.1: SEM-EDS elemental composition analysis for 10-minute reaction time sample comprising raw atomic percentages and relative atomic percentages solely considering Cs, Na, Yb, and Cl.

PL spectra were collected for each sample (Figure 3.3) and all look qualitatively similar exhibiting an emission maximum centered around $\lambda_{em} \approx 430$ nm (peak arising at $\lambda_{em} \approx 410$ nm is attributed to Raman scattering of the solvent toluene). The quantum yields of each sample were calculated as 2.59, 2.52, 3.61, and 2.39 % for the 5-second, 1-, 5-, and 10-minute samples, respectively. These quantum yields are quite low compared to typical all-inorganic lead halide nanocrystals but are characteristic of double perovskites.[169, 175-177] Single lead halide perovskites generally exhibit a direct bandgap as a result of the nature of the band edge transition, which is typically a halide *p*- to lead *p*-orbital transition.[49] Though there is some variety possible with lead halide perovskites, the nature of the BX_6 octahedra is well defined and this is what governs the electronic structure of the material. In the case of DPs, each one unit cell has two different types

of BX_6 octahedra owing to the presence of two different B-site cations. As a result, the electronic structure can vary as the band edge transition is a metal-to-metal charge transfer (MMCT) which is dependent on the highest-occupied molecular orbital (HOMO) and lowest unoccupied molecular orbital (LUMO) of both BX_6 octahedra, resulting in the possibility for the material to have a direct *or* indirect bandgap.[104] As such, there is much interest in being able to modulate the electronic structure of double perovskites to endow them with more favourable electronic properties for their intended applications.

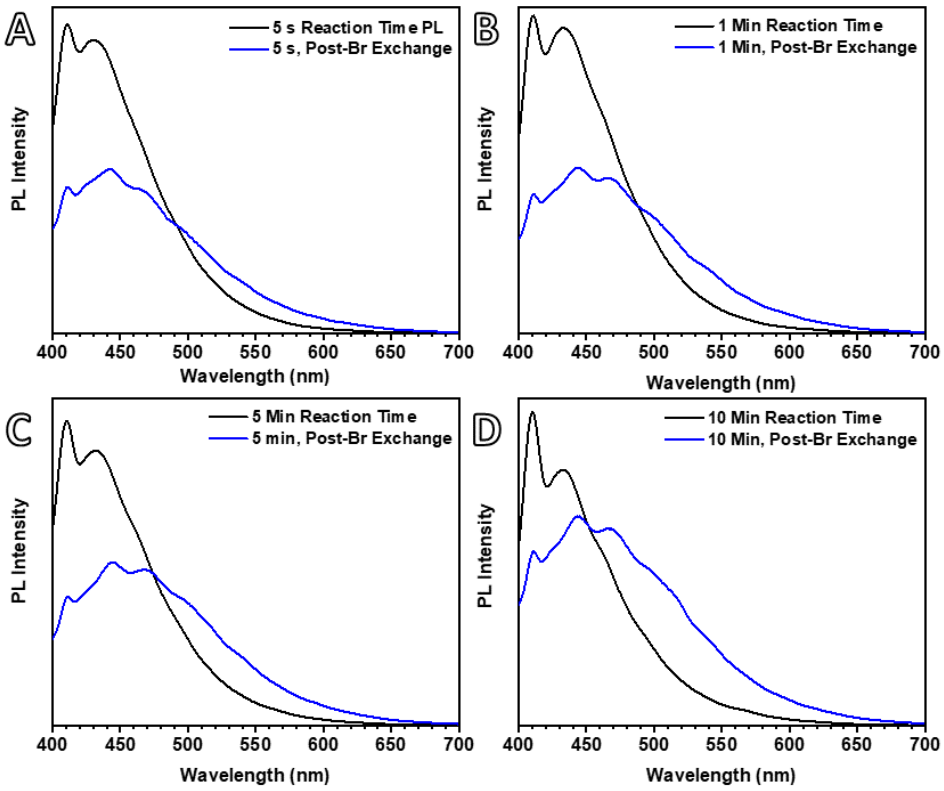

Figure 3.3: Photoluminescence spectra of $Cs_2NaYbCl_6$ nanoparticles synthesized with (A) 5-second, (B) 1-, (C) 5-, and (D) 10-minute reaction times, measured before and after ion-exchange with OLAM-Br. (All samples were dispersed in toluene with λ_{ex} = 365 nm)

One such way is in tuning the chemical composition, which can be done *in situ* or post-synthetically.[96, 109, 178-179] In this work, we attempted to accomplish this *via* the post-synthetic anion-exchange of our synthesized NCs. Samples were exposed to OLAM-Br and OLAM-I dissolved in toluene, and the resulting PL spectra of the Br-exchanged samples were recorded (Figure 3.3). A noticeable change in PL spectrum is observed across all samples, resulting in decreased intensity of the initial peak at λ_{em} = 430 nm turning it into a shoulder, and the generation of new peaks/shoulders at ~444, ~467, and ~490 nm. These new signals are notably all separated by 23 nm and are reminiscent of a vibronic series, though this is uncommon in photoluminescence of perovskite materials and so it is unclear whether this is pure coincidence. The series of PL peaks may be due to multiple phases present in the samples experiencing the bromide exchange and producing varying morphologies, each with their distinct emission. The exchange with OLAM-I resulted in a solution that was barely photoluminescent and was unsuccessful, likely due to the large difference in size of the iodide ion compared to the chloride ion, causing too great a change in crystal lattice and possibly destroying the NCs present in the conversion solution.

3.3 Conclusion

In this work, there is evidence suggesting the first successful synthesis of $Cs_2NaYbCl_6$ DP NCs. TEM confirms the presence of NCs resulting from a hot-injection synthetic method. The as-synthesized NCs display a PL peak centered around 430 nm with quantum yields of approximately 2-3 %. Compositional analysis *via* SEM-EDS confirmed, qualitatively, the presence of the expected ions in the analysed samples. These NCs were exposed post-synthetically to OLAM-Br to trigger anion-exchange towards $Cs_2NaYbBr_6$, resulting in the generation of a series of PL peaks/shoulders spaced approximately 23 nm apart. This may hint at the conversion of multiple

phases in the sample to various bromide-containing species, each with a distinct emission. This work serves as a launch point from which much more work can be done to ascertain the exact nature of the resultant DP NCs. The synthetic procedure can be optimized from the adapted method to produce a more phase-pure material, possibly by performing the reaction at higher temperatures. Further modification of the electronic structure of the $Cs_2NaYbCl_6$ can also be explored *via* doping or alloying, as well as further investigation into anion-exchange. Efforts in these directions can lead to the optimization of a novel, lead-free perovskite material which can prove useful in applications of solar energy conversion.

Chapter 4: Conclusion and Outlook

In the present work, a synthetic method for electrochemically depositing microstructures of aragonite $CaCO_3$ and converting them to $CsPbBr_3$ *via* ion-exchange reactions was proposed. Conversion resulted in layered microstructures as conversion to $PbCO_3$ was achieved on the surface of the microstructures without full penetration and conversion. The final conversion led to the growth of $CsPbBr_3$ nanocrystals from the $PbCO_3$ layer of the microstructures, resulting in a stratified structure. This work demonstrates a novel way in which to control bulk morphology of a perovskite-containing material. Conversion of metal carbonate microstructures to perovskite has been previously reported, though this was done with metal carbonates coprecipitated with SiO_2 which served as a scaffold, and was done to convert to the hybrid organic-inorganic perovskite $MAPbI_3$. The present work represents the unique case of using pure metal carbonate microstructures as a template for conversion to an all-inorganic perovskite. In using electrochemical deposition as the method for generating these microstructures, a greater degree of control and reproducibility are achieved versus traditional crystal growth methods.

The synthetic procedure was extended to the direct synthesis of the corresponding chloride and iodide cesium lead halides, resulting in microstructures of $CsPbCl_3$ which adhered to expected optical properties for nanocrystals of $CsPbCl_3$. The resulting iodide diverged significantly from expected photoluminescence, possibly owing to its lower ease of formation.

The $CsPbBr_3$ microstructures modified by post-synthetic anion-exchange, resulting in mixed halide perovskites $CsPbBr_{3-x}Cl_x$ and $CsPbBr_{3-x}I_x$, showing that the proposed synthetic method can be built upon to tune the resulting materials to any point in the visible light spectrum.

This work represents a unique and interesting case of perovskite synthesis where the resulting nanocrystals of $CsPbX_3$ are likely without organic capping group, though further characterization would be required to ascertain this. However, the only possible capping group that could be present is methanol, which differs significantly from typical long-chain capping molecules. This leads to two interesting avenues of future work: further characterization of the surface perovskite layer to determine the presence or absence of capping groups, and the incorporation of new organic capping groups as a way to stabilize and possibly optoelectronically enhance the perovskite microstructures.

A synthetic method was also adapted for the synthesis of novel $Cs_2NaYbCl_6$ double perovskite nanocrystals. Using a hot-injection method, nanocrystals were synthesized and were seen to exhibit an emission maximum of $\lambda_{em} = 430$ nm. The synthesis was performed with varying reaction times to observe the effect on particle size and phase purity, and while a negligible effect was observed on the particle size, the phases differed at each time interval tested. The 1-minute reaction time resulted in cubic nanoparticles with well-defined vertices, characteristic of perovskite nanomaterials. The synthesized materials exhibited low photoluminescence quantum yields of approximately 2-3 %, which is typical of double perovskites which often have indirect bandgaps. As such, anion-exchange was performed as the change in chemical composition can result in the modulation of a perovskite material's electronic structure and properties. Bromide anion exchange resulted in the generation of a series new emission peaks separated approximately 23 nm apart, potentially signaling the conversion of multiple phases present in the sample to bromide-containing species.

This work serves as a launching point for future investigation and characterization of $Cs_2NaYbCl_6$ nanomaterials, as well as the exploration of different ways in which the electronic structure can be modified to enhance the material's optoelectronic properties.

References

1. Lux, S.; Baldauf-Sommerbauer, G.; Siebenhofer, M. Hydrogenation of Inorganic Metal Carbonates: A Review on Its Potential for Carbon Dioxide Utilization and Emission Reduction. *ChemSusChem* **2018,** *11* (19), 3357-3375.
2. Castanier, S.; Le Métayer-Levrel, G.; Perthuisot, J.-P. Ca-carbonates precipitation and limestone genesis — the microbiogeologist point of view. *Sediment. Geol.* **1999,** *126* (1), 9-23.
3. Ehrlich, H. L. Geomicrobiology: its significance for geology. *Earth Sci. Rev.* **1998,** *45* (1), 45-60.
4. Hammes, F.; Verstraete*, W. Key roles of pH and calcium metabolism in microbial carbonate precipitation. *Rev. Environ. Sci. Biotechnol.* **2002,** *1* (1), 3-7.
5. Douglas, S.; Beveridge, T. J. Mineral formation by bacteria in natural microbial communities. *FEMS Microbiol. Ecol.* **1998,** *26* (2), 79-88.
6. Feng, Q., Principles of Calcium-Based Biomineralization. In *Molecular Biomineralization: Aquatic Organisms Forming Extraordinary Materials*, Müller, W. E. G., Ed. Springer Berlin Heidelberg: Berlin, Heidelberg, 2011; pp 141-197.
7. Feng, Q. L.; Li, H. B.; Pu, G.; Zhang, D. M.; Cui, F. Z.; Li, H. D.; Kim, T. N. Crystallographic alignment of calcite prisms in the oblique prismatic layer of Mytilus edulis shell. *J. Mater. Sci.* **2000,** *35* (13), 3337-3340.
8. Ramakrishna, C.; Thenepalli, T.; Ahn, J.-W. A Brief review of Aragonite Precipitated Calcium Carbonate (PCC) Synthesis Methods and Its Applications. *Korean Chem. Eng. Res* **2017,** *55* (4), 443-455.
9. Sommerdijk, N. A. J. M.; With, G. d. Biomimetic CaCO3 Mineralization using Designer Molecules and Interfaces. *Chem. Rev.* **2008,** *108* (11), 4499-4550.
10. Gabrielli, C.; Jaouhari, R.; Joiret, S.; Maurin, G.; Rousseau, P. Study of the Electrochemical Deposition of $CaCO_3$ by In Situ Raman Spectroscopy. *J. Electrochem. Soc.* **2003,** *150* (7), C478.
11. Dirany, A.; Drogui, P.; El Khakani, M. A. Clean electrochemical deposition of calcium carbonate to prevent scale formation in cooling water systems. *Environ. Chem. Lett.* **2016,** *14* (4), 507-514.
12. Kulp, E. A.; Switzer, J. A. Electrochemical Biomineralization: The Deposition of Calcite with Chiral Morphologies. *J. Am. Chem. Soc.* **2007,** *129* (49), 15120-15121.
13. Souiad, F.; Bendaoud-Boulahlib, Y.; Rodrigues, A. S.; Fernandes, A.; Ciríaco, L.; Pacheco, M. J.; Lopes, A. Electrodeposition of Calcium Carbonate and Magnesium Carbonate from Hard Water on Stainless-Steel Electrode to Prevent Natural Scaling Phenomenon. *Water* **2021,** *13* (19), 2752.
14. Kamyshny, A.; Magdassi, S. Conductive Nanomaterials for Printed Electronics. *Small* **2014,** *10* (17), 3515-3535.
15. Wu, W. Inorganic nanomaterials for printed electronics: a review. *Nanoscale* **2017,** *9* (22), 7342-7372.
16. Wang, S.; Wang, L.; Huang, W. Bismuth-based photocatalysts for solar energy conversion. *J. Mater. Chem. A* **2020,** *8* (46), 24307-24352.
17. Zheng, X.; Zhang, L. Photonic nanostructures for solar energy conversion. *Energy Environ. Sci.* **2016,** *9* (8), 2511-2532.
18. Iqbal, W.; Yang, B.; Zhao, X.; Rauf, M.; Waqas, M.; Gong, Y.; Zhang, J.; Mao, Y. Controllable synthesis of graphitic carbon nitride nanomaterials for solar energy conversion and

environmental remediation: the road travelled and the way forward. *Catal. Sci. Technol.* **2018,** *8* (18), 4576-4599.
19. Mei, X.; Hu, T.; Wang, Y.; Weng, X.; Liang, R.; Wei, M. Recent advancements in two-dimensional nanomaterials for drug delivery. *Wiley Interdiscip. Rev. Nanomed. Nanobiotechnol.* **2020,** *12* (2), e1596.
20. Fernandez-Fernandez, A.; Manchanda, R.; McGoron, A. J. Theranostic Applications of Nanomaterials in Cancer: Drug Delivery, Image-Guided Therapy, and Multifunctional Platforms. *Appl. Biochem. Biotechnol.* **2011,** *165* (7), 1628-1651.
21. Tetsuka, H.; Asahi, R.; Nagoya, A.; Okamoto, K.; Tajima, I.; Ohta, R.; Okamoto, A. Optically Tunable Amino-Functionalized Graphene Quantum Dots. *Adv. Mater.* **2012,** *24* (39), 5333-5338.
22. Chuang, P.-H.; Lin, C. C.; Liu, R.-S. Emission-Tunable CuInS2/ZnS Quantum Dots: Structure, Optical Properties, and Application in White Light-Emitting Diodes with High Color Rendering Index. *ACS Appl. Mater. Interfaces* **2014,** *6* (17), 15379-15387.
23. Fichtner, J.; Watzele, S.; Garlyyev, B.; Kluge, R. M.; Haimerl, F.; El-Sayed, H. A.; Li, W.-J.; Maillard, F. M.; Dubau, L.; Chattot, R.; Michalička, J.; Macak, J. M.; Wang, W.; Wang, D.; Gigl, T.; Hugenschmidt, C.; Bandarenka, A. S. Tailoring the Oxygen Reduction Activity of Pt Nanoparticles through Surface Defects: A Simple Top-Down Approach. *ACS Catal.* **2020,** *10* (5), 3131-3142.
24. Xing, H.; Bai, Y.; Bai, Y.; Tan, L. H.; Tao, J.; Pedretti, B.; Vincil, G. A.; Lu, Y.; Zimmerman, S. C. Bottom-Up Strategy To Prepare Nanoparticles with a Single DNA Strand. *J. Am. Chem. Soc.* **2017,** *139* (10), 3623-3626.
25. Wang, Y.; Xia, Y. Bottom-Up and Top-Down Approaches to the Synthesis of Monodispersed Spherical Colloids of Low Melting-Point Metals. *Nano Lett.* **2004,** *4* (10), 2047-2050.
26. Jia, X.; Khan, W.; Wu, Z.; Choi, J.; Yip, A. C. K. Modern synthesis strategies for hierarchical zeolites: Bottom-up versus top-down strategies. *Adv. Powder Technol.* **2019,** *30* (3), 467-484.
27. Luechinger, N. A.; Grass, R. N.; Athanassiou, E. K.; Stark, W. J. Bottom-up Fabrication of Metal/Metal Nanocomposites from Nanoparticles of Immiscible Metals. *Chem. Mater.* **2010,** *22* (1), 155-160.
28. Sun, H.; Ji, H.; Ju, E.; Guan, Y.; Ren, J.; Qu, X. Synthesis of Fluorinated and Nonfluorinated Graphene Quantum Dots through a New Top-Down Strategy for Long-Time Cellular Imaging. *Chem. Eur. J.* **2015,** *21* (9), 3791-3797.
29. Amano, F.; Nogami, K.; Tanaka, M.; Ohtani, B. Correlation between Surface Area and Photocatalytic Activity for Acetaldehyde Decomposition over Bismuth Tungstate Particles with a Hierarchical Structure. *Langmuir* **2010,** *26* (10), 7174-7180.
30. Rossetti, R.; Ellison, J. L.; Gibson, J. M.; Brus, L. E. Size effects in the excited electronic states of small colloidal CdS crystallites. *J. Chem. Phys.* **1984,** *80* (9), 4464-4469.
31. Brus, L. Electronic wave functions in semiconductor clusters: experiment and theory. *J. Phys. Chem.* **1986,** *90* (12), 2555-2560.
32. Wu, J.; Chen, S.; Seeds, A.; Liu, H. Quantum dot optoelectronic devices: lasers, photodetectors and solar cells. *J. Phys. D: Appl. Phys.* **2015,** *48* (36), 363001.
33. Protesescu, L.; Yakunin, S.; Bodnarchuk, M. I.; Krieg, F.; Caputo, R.; Hendon, C. H.; Yang, R. X.; Walsh, A.; Kovalenko, M. V. Nanocrystals of Cesium Lead Halide Perovskites ($CsPbX_3$, X = Cl, Br, and I): Novel Optoelectronic Materials Showing Bright Emission with Wide Color Gamut. *Nano Lett.* **2015,** *15* (6), 3692-3696.
34. Akkerman, Q. A.; Manna, L. What Defines a Halide Perovskite? *ACS Energy Lett.* **2020,** *5* (2), 604-610.

35. Chakhmouradian, A. R.; Woodward, P. M. Celebrating 175 years of perovskite research: a tribute to Roger H. Mitchell. *Phys. Chem. Miner.* **2014,** *41* (6), 387-391.
36. Castellano, C.; Russo, M. Parascandolaite, $KMgF_3$, a new perovskitetype fluoride from Vesuvius. *Phys. Chem. Miner.* **2014,** *41* (6), 403-407.
37. Stoumpos, C. C.; Kanatzidis, M. G. The Renaissance of Halide Perovskites and Their Evolution as Emerging Semiconductors. *Acc. Chem. Res.* **2015,** *48* (10), 2791-2802.
38. Volonakis, G.; Filip, M. R.; Haghighirad, A. A.; Sakai, N.; Wenger, B.; Snaith, H. J.; Giustino, F. Lead-Free Halide Double Perovskites via Heterovalent Substitution of Noble Metals. *J. Phys. Chem. Lett.* **2016,** *7* (7), 1254-1259.
39. Maughan, A. E.; Ganose, A. M.; Scanlon, D. O.; Neilson, J. R. Perspectives and Design Principles of Vacancy-Ordered Double Perovskite Halide Semiconductors. *Chem. Mater.* **2019,** *31* (4), 1184-1195.
40. Goldschmidt, V. M. Die gesetze der krystallochemie. *Sci. Nat.* **1926,** *14* (21), 477-485.
41. Kudo, A.; Miseki, Y. Heterogeneous photocatalyst materials for water splitting. *Chem. Soc. Rev.* **2009,** *38* (1), 253-278.
42. Tschauner, O.; Huang, S.; Yang, S.; Humayun, M.; Liu, W.; Corder, S. N. G.; Bechtel, H. A.; Tischler, J.; Rossman, G. R. Discovery of davemaoite, $CaSiO_3$-perovskite, as a mineral from the lower mantle. *Science* **2021,** *374* (6569), 891-894.
43. Zeng, S.; Kar, P.; Thakur, U. K.; Shankar, K. A review on photocatalytic CO_2 reduction using perovskite oxide nanomaterials. *Nanotechnology* **2018,** *29* (5), 052001.
44. Wells, H. L. Über die cäsium-und kalium-bleihalogenide. *Z. Anorg. Allg. Chem.* **1893,** *3* (1), 195-210.
45. MØLler, C. K. A Phase Transition in Cæsium Plumbochloride. *Nature* **1957,** *180* (4593), 981-982.
46. Weber, D. $CH_3NH_3PbX_3$, ein Pb(II)-System mit kubischer Perowskitstruktur / $CH_3NH_3PbX_3$, a Pb(II)-System with Cubic Perovskite Structure. *Z. Naturforsch. B* **1978,** *33* (12), 1443-1445.
47. Weber, D. $CH_3NH_3SnBr_xI_{3-x}$ (x = 0-3), ein Sn(II)-System mit kubischer Perowskitstruktur / $CH_3NH_3SnBr_xI_{3-x}$(x = 0-3), a Sn(II)-System with Cubic Perovskite Structure. *Z. Naturforsch. B* **1978,** *33* (8), 862-865.
48. Kojima, A.; Teshima, K.; Shirai, Y.; Miyasaka, T. Organometal Halide Perovskites as Visible-Light Sensitizers for Photovoltaic Cells. *J. Am. Chem. Soc.* **2009,** *131* (17), 6050-6051.
49. Yin, W.-J.; Shi, T.; Yan, Y. Unique Properties of Halide Perovskites as Possible Origins of the Superior Solar Cell Performance. *Adv. Mater.* **2014,** *26* (27), 4653-4658.
50. Chung, I.; Lee, B.; He, J.; Chang, R. P. H.; Kanatzidis, M. G. All-solid-state dye-sensitized solar cells with high efficiency. *Nature* **2012,** *485* (7399), 486-489.
51. Noel, N. K.; Stranks, S. D.; Abate, A.; Wehrenfennig, C.; Guarnera, S.; Haghighirad, A.-A.; Sadhanala, A.; Eperon, G. E.; Pathak, S. K.; Johnston, M. B. Lead-free organic–inorganic tin halide perovskites for photovoltaic applications. *Energy Environ. Sci.* **2014,** *7* (9), 3061-3068.
52. Ito, N.; Kamarudin, M. A.; Hirotani, D.; Zhang, Y.; Shen, Q.; Ogomi, Y.; Iikubo, S.; Minemoto, T.; Yoshino, K.; Hayase, S. Mixed Sn–Ge Perovskite for Enhanced Perovskite Solar Cell Performance in Air. *J. Phys. Chem. Lett.* **2018,** *9* (7), 1682-1688.
53. Sun, P.-P.; Li, Q.-S.; Yang, L.-N.; Li, Z.-S. Theoretical insights into a potential lead-free hybrid perovskite: substituting Pb^{2+} with Ge^{2+}. *Nanoscale* **2016,** *8* (3), 1503-1512.
54. Richardson, G.; O'Kane, S. E.; Niemann, R. G.; Peltola, T. A.; Foster, J. M.; Cameron, P. J.; Walker, A. B. Can slow-moving ions explain hysteresis in the current–voltage curves of perovskite solar cells? *Energy Environ. Sci.* **2016,** *9* (4), 1476-1485.

55. Grancini, G.; Roldán-Carmona, C.; Zimmermann, I.; Mosconi, E.; Lee, X.; Martineau, D.; Narbey, S.; Oswald, F.; De Angelis, F.; Graetzel, M.; Nazeeruddin, M. K. One-Year stable perovskite solar cells by 2D/3D interface engineering. *Nat. Commun.* **2017,** *8*, 15684.
56. Yang, J.; Siempelkamp, B. D.; Liu, D.; Kelly, T. L. Investigation of $CH_3NH_3PbI_3$ Degradation Rates and Mechanisms in Controlled Humidity Environments Using in Situ Techniques. *ACS Nano* **2015,** *9* (2), 1955-1963.
57. Leguy, A. M. A.; Hu, Y.; Campoy-Quiles, M.; Alonso, M. I.; Weber, O. J.; Azarhoosh, P.; van Schilfgaarde, M.; Weller, M. T.; Bein, T.; Nelson, J.; Docampo, P.; Barnes, P. R. F. Reversible Hydration of $CH_3NH_3PbI_3$ in Films, Single Crystals, and Solar Cells. *Chem. Mater.* **2015,** *27* (9), 3397-3407.
58. Schmitz, A.; Montanarella, F.; Schaberg, L. L.; Abdelbaky, M.; Kovalenko, M. V.; Bacher, G. Optical Probing of Crystal Lattice Configurations in Single $CsPbBr_3$ Nanoplatelets. *Nano Lett.* **2021,** *21* (21), 9085-9092.
59. Eperon, G. E.; Paternò, G. M.; Sutton, R. J.; Zampetti, A.; Haghighirad, A. A.; Cacialli, F.; Snaith, H. J. Inorganic caesium lead iodide perovskite solar cells. *J. Mater. Chem. A* **2015,** *3* (39), 19688-19695.
60. Akkerman, Q. A.; Gandini, M.; Di Stasio, F.; Rastogi, P.; Palazon, F.; Bertoni, G.; Ball, J. M.; Prato, M.; Petrozza, A.; Manna, L. Strongly emissive perovskite nanocrystal inks for high-voltage solar cells. *Nat. Energy* **2016,** *2* (2), 16194.
61. Manser, J. S.; Christians, J. A.; Kamat, P. V. Intriguing Optoelectronic Properties of Metal Halide Perovskites. *Chem. Rev.* **2016,** *116* (21), 12956-13008.
62. Ran, C.; Xu, J.; Gao, W.; Huang, C.; Dou, S. Defects in metal triiodide perovskite materials towards high-performance solar cells: origin, impact, characterization, and engineering. *Chem. Soc. Rev.* **2018,** *47* (12), 4581-4610.
63. Steirer, K. X.; Schulz, P.; Teeter, G.; Stevanovic, V.; Yang, M.; Zhu, K.; Berry, J. J. Defect Tolerance in Methylammonium Lead Triiodide Perovskite. *ACS Energy Lett.* **2016,** *1* (2), 360-366.
64. Li, J.; Xu, L.; Wang, T.; Song, J.; Chen, J.; Xue, J.; Dong, Y.; Cai, B.; Shan, Q.; Han, B.; Zeng, H. 50-Fold EQE Improvement up to 6.27% of Solution-Processed All-Inorganic Perovskite $CsPbBr_3$ QLEDs via Surface Ligand Density Control. *Adv. Mater.* **2017,** *29* (5), 1603885.
65. Pan, J.; Shang, Y.; Yin, J.; De Bastiani, M.; Peng, W.; Dursun, I.; Sinatra, L.; El-Zohry, A. M.; Hedhili, M. N.; Emwas, A.-H.; Mohammed, O. F.; Ning, Z.; Bakr, O. M. Bidentate Ligand-Passivated $CsPbI_3$ Perovskite Nanocrystals for Stable Near-Unity Photoluminescence Quantum Yield and Efficient Red Light-Emitting Diodes. *J. Am. Chem. Soc.* **2018,** *140* (2), 562-565.
66. Xie, Q.; Wu, D.; Wang, X.; Li, Y.; Fang, F.; Wang, Z.; Ma, Y.; Su, M.; Peng, S.; Liu, H.; Wang, K.; Sun, X. W. Branched capping ligands improve the stability of cesium lead halide ($CsPbBr_3$) perovskite quantum dots. *J. Mater. Chem. C* **2019,** *7* (36), 11251-11257.
67. Krieg, F.; Ochsenbein, S. T.; Yakunin, S.; ten Brinck, S.; Aellen, P.; Süess, A.; Clerc, B.; Guggisberg, D.; Nazarenko, O.; Shynkarenko, Y.; Kumar, S.; Shih, C.-J.; Infante, I.; Kovalenko, M. V. Colloidal $CsPbX_3$ (X = Cl, Br, I) Nanocrystals 2.0: Zwitterionic Capping Ligands for Improved Durability and Stability. *ACS Energy Lett.* **2018,** *3* (3), 641-646.
68. Akkerman, Q. A.; D'Innocenzo, V.; Accornero, S.; Scarpellini, A.; Petrozza, A.; Prato, M.; Manna, L. Tuning the Optical Properties of Cesium Lead Halide Perovskite Nanocrystals by Anion Exchange Reactions. *J. Am. Chem. Soc.* **2015,** *137* (32), 10276-10281.

69. Nedelcu, G.; Protesescu, L.; Yakunin, S.; Bodnarchuk, M. I.; Grotevent, M. J.; Kovalenko, M. V. Fast Anion-Exchange in Highly Luminescent Nanocrystals of Cesium Lead Halide Perovskites ($CsPbX_3$, X = Cl, Br, I). *Nano Lett.* **2015,** *15* (8), 5635-5640.
70. Shamsi, J.; Dang, Z.; Bianchini, P.; Canale, C.; Di Stasio, F.; Brescia, R.; Prato, M.; Manna, L. Colloidal Synthesis of Quantum Confined Single Crystal $CsPbBr_3$ Nanosheets with Lateral Size Control up to the Micrometer Range. *J. Am. Chem. Soc.* **2016,** *138* (23), 7240-7243.
71. He, J.; Towers, A.; Wang, Y.; Yuan, P.; Jiang, Z.; Chen, J.; Gesquiere, A. J.; Wu, S.-T.; Dong, Y. In situ synthesis and macroscale alignment of $CsPbBr_3$ perovskite nanorods in a polymer matrix. *Nanoscale* **2018,** *10* (33), 15436-15441.
72. Tian, C.; Wang, F.; Wang, Y.; Yang, Z.; Chen, X.; Mei, J.; Liu, H.; Zhao, D. Chemical Vapor Deposition Method Grown All-Inorganic Perovskite Microcrystals for Self-Powered Photodetectors. *ACS Appl. Mater. Interfaces* **2019,** *11* (17), 15804-15812.
73. Mo, X.; Li, X.; Dai, G.; He, P.; Sun, J.; Huang, H.; Yang, J. All-inorganic perovskite $CsPbBr_3$ microstructures growth via chemical vapor deposition for high-performance photodetectors. *Nanoscale* **2019,** *11* (44), 21386-21393.
74. Lan, S.; Li, W.; Wang, S.; Li, J.; Wang, J.; Wang, H.; Luo, H.; Li, D. Vapor-Phase Growth of $CsPbBr_3$ Microstructures for Highly Efficient Pure Green Light Emission. *Adv. Opt. Mater.* **2019,** *7* (2), 1801336.
75. Cross, C. W.; Hillebrand, W. F. On minerals of the cryolite group recently found in Colorado. *Am. J. Sci.* **1883,** *s3-26* (154), 271-294.
76. Cross, W.; Hillebrand, W. F., *Contributions to the mineralogy of the Rocky Mountains*. US Government Printing Office: 1885.
77. Menzer, G. Über die Kristallstrukturen der Kryolithgruppe. *Fortschr. Miner* **1932,** *17*, 61.
78. Wells, H. L. Some complex chlorides containing gold. *Am. J. Sci.* **1922,** *s5-3* (17), 315-326.
79. Elliott, N.; Pauling, L. The Crystal Structure of Cesium Aurous Auric Chloride, $Cs_2AuAuCl_6$, and Cesium Argentous Auric Chloride, $Cs_2AgAuCl_6$. *J. Am. Chem. Soc.* **1938,** *60* (8), 1846-1851.
80. Knox, K.; Mitchell, D. W. The preparation and structure of K_2NaCrF_6, K_2NaFeF_6 and K_2NaGaF_6. *J. Inorg. Nucl. Chem.* **1961,** *21* (3), 253-258.
81. Morss, L. R.; Siegal, M.; Stenger, L.; Edelstein, N. Preparation of cubic chloro complex compounds of trivalent metals: Cs_2NaMCl_6. *Inorg. Chem.* **1970,** *9* (7), 1771-1775.
82. Meyer, G. The synthesis and structures of complex rare-earth halides. *Prog. Solid State Chem.* **1982,** *14* (3), 141-219.
83. Bucher, E.; Guggenheim, H. J.; Andres, K.; Hull, G. W.; Cooper, A. S. Magnetic properties of some cubic rare-earth elpasolite hexafluorides. *Phys. Rev. B* **1974,** *10* (7), 2945-2951.
84. Amberger, H. D.; Rosenbauer, G. G.; Fischer, R. D. The electronic structure of highly-symmetrical compounds of the lanthanides and actinides—VII: The electronic Raman spectra of the lanthanide elpasolites of the type $Cs_2NaLn(III)Cl_6$. *J. Phys. Chem. Solids* **1977,** *38* (4), 379-385.
85. Dunlap, B. D.; Shenoy, G. K.; Dattagupta, S.; Asch, L. Paramagnetic spin relaxation in $Cs_2NaYbCl_6$. *Physica B+C* **1977,** *86-88*, 1267-1268.
86. Gamelin, D. R.; Güdel, H. U. Two-Photon Spectroscopy of d3 Transition Metals: Near-IR-to-Visible Upconversion Luminescence by Re^{4+} and Mo^{3+}. *J. Am. Chem. Soc.* **1998,** *120* (46), 12143-12144.

87. Reber, C.; Guedel, H. U.; Meyer, G.; Schleid, T.; Daul, C. A. Optical spectroscopic and structural properties of vanadium^{3+}-doped fluoride, chloride, and bromide elpasolite lattices. *Inorg. Chem.* **1989,** *28* (16), 3249-3258.
88. Combes, C. M.; Dorenbos, P.; van Eijk, C. W. E.; Krämer, K. W.; Güdel, H. U. Optical and scintillation properties of pure and Ce^{3+}-doped Cs_2LiYCl_6 and Li_3YCl_6:Ce^{3+} crystals. *J. Lumin.* **1999,** *82* (4), 299-305.
89. Shoichiro, Y.; Ryutaro, T. Spectrochemical Study of Microscopic Crystals. XI. The Structure and Polarized Absorption Spectra of Some Metallic Compounds with Remarkable Interaction between Metal Atoms through Anions. *Bull. Chem. Soc. Jpn.* **1956,** *29* (3), 421-425.
90. Brauer, G.; Sleater, G. Preparation of mixed valent aurate halides. *J. Less Common Met.* **1970,** *21* (3), 283-291.
91. Lee, B.; Stoumpos, C. C.; Zhou, N.; Hao, F.; Malliakas, C.; Yeh, C.-Y.; Marks, T. J.; Kanatzidis, M. G.; Chang, R. P. H. Air-Stable Molecular Semiconducting Iodosalts for Solar Cell Applications: Cs_2SnI_6 as a Hole Conductor. *J. Am. Chem. Soc.* **2014,** *136* (43), 15379-15385.
92. Cai, Y.; Xie, W.; Teng, Y. T.; Harikesh, P. C.; Ghosh, B.; Huck, P.; Persson, K. A.; Mathews, N.; Mhaisalkar, S. G.; Sherburne, M.; Asta, M. High-throughput Computational Study of Halide Double Perovskite Inorganic Compounds. *Chem. Mater.* **2019,** *31* (15), 5392-5401.
93. Rai, D. P.; Shankar, A.; Ghimire, M. P.; Sandeep; Thapa, R. K. The electronic, magnetic and optical properties of double perovskite A_2FeReO_6 (A=Sr, Ba) from first principles approach. *Comput. Mater. Sci.* **2015,** *101*, 313-320.
94. Deng, Z.; Wei, F.; Sun, S.; Kieslich, G.; Cheetham, A. K.; Bristowe, P. D. Exploring the properties of lead-free hybrid double perovskites using a combined computational-experimental approach. *J. Mater. Chem. A* **2016,** *4* (31), 12025-12029.
95. Slavney, A. H.; Hu, T.; Lindenberg, A. M.; Karunadasa, H. I. A Bismuth-Halide Double Perovskite with Long Carrier Recombination Lifetime for Photovoltaic Applications. *J. Am. Chem. Soc.* **2016,** *138* (7), 2138-2141.
96. McClure, E. T.; Ball, M. R.; Windl, W.; Woodward, P. M. Cs_2AgBiX_6 (X = Br, Cl): New Visible Light Absorbing, Lead-Free Halide Perovskite Semiconductors. *Chem. Mater.* **2016,** *28* (5), 1348-1354.
97. Idris, A. M.; Liu, T.; Hussain Shah, J.; Malik, A. S.; Zhao, D.; Han, H.; Li, C. Sr_2NiWO_6 Double Perovskite Oxide as a Novel Visible-Light-Responsive Water Oxidation Photocatalyst. *ACS Appl. Mater. Interfaces* **2020,** *12* (23), 25938-25948.
98. Zhang, Z.; Liang, Y.; Huang, H.; Liu, X.; Li, Q.; Chen, L.; Xu, D. Stable and Highly Efficient Photocatalysis with Lead-Free Double-Perovskite of $Cs_2AgBiBr_6$. *Angew. Chem. Int. Ed.* **2019,** *58* (22), 7263-7267.
99. Wang, J.; Pan, F.; Wong, K.-L.; Tanner, P. A. Unexpected 700 nm upconversion emission for $Cs_2NaYbCl_6$ and its co-doped hexachloroelpasolites. *J. Lumin.* **2019,** *211*, 20-25.
100. Xu, Y.; Jiao, B.; Song, T.-B.; Stoumpos, C. C.; He, Y.; Hadar, I.; Lin, W.; Jie, W.; Kanatzidis, M. G. Zero-Dimensional Cs_2TeI_6 Perovskite: Solution-Processed Thick Films with High X-ray Sensitivity. *ACS Photonics* **2019,** *6* (1), 196-203.
101. Locardi, F.; Cirignano, M.; Baranov, D.; Dang, Z.; Prato, M.; Drago, F.; Ferretti, M.; Pinchetti, V.; Fanciulli, M.; Brovelli, S.; De Trizio, L.; Manna, L. Colloidal Synthesis of Double Perovskite $Cs_2AgInCl_6$ and Mn-Doped $Cs_2AgInCl_6$ Nanocrystals. *J. Am. Chem. Soc.* **2018,** *140* (40), 12989-12995.
102. Lamba, R. S.; Basera, P.; Bhattacharya, S.; Sapra, S. Band Gap Engineering in $Cs_2(Na_xAg_{1-x})BiCl_6$ Double Perovskite Nanocrystals. *J. Phys. Chem. Lett.* **2019,** *10* (17), 5173-5181.

103. Yang, B.; Mao, X.; Hong, F.; Meng, W.; Tang, Y.; Xia, X.; Yang, S.; Deng, W.; Han, K. Lead-Free Direct Band Gap Double-Perovskite Nanocrystals with Bright Dual-Color Emission. *J. Am. Chem. Soc.* **2018,** *140* (49), 17001-17006.
104. Slavney, A. H.; Connor, B. A.; Leppert, L.; Karunadasa, H. I. A pencil-and-paper method for elucidating halide double perovskite band structures. *Chem. Sci.* **2019,** *10* (48), 11041-11053.
105. Brivio, F.; Butler, K. T.; Walsh, A.; van Schilfgaarde, M. Relativistic quasiparticle self-consistent electronic structure of hybrid halide perovskite photovoltaic absorbers. *Phys. Rev. B* **2014,** *89* (15), 155204.
106. Wang, Y.; Gould, T.; Dobson, J. F.; Zhang, H.; Yang, H.; Yao, X.; Zhao, H. Density functional theory analysis of structural and electronic properties of orthorhombic perovskite $CH_3NH_3PbI_3$. *Phys. Chem. Chem. Phys.* **2014,** *16* (4), 1424-1429.
107. Slavney, A. H.; Leppert, L.; Saldivar Valdes, A.; Bartesaghi, D.; Savenije, T. J.; Neaton, J. B.; Karunadasa, H. I. Small-Band-Gap Halide Double Perovskites. *Angew. Chem. Int. Ed.* **2018,** *57* (39), 12765-12770.
108. Tran, T. T.; Panella, J. R.; Chamorro, J. R.; Morey, J. R.; McQueen, T. M. Designing indirect–direct bandgap transitions in double perovskites. *Mater. Horiz.* **2017,** *4* (4), 688-693.
109. Creutz, S. E.; Crites, E. N.; De Siena, M. C.; Gamelin, D. R. Colloidal Nanocrystals of Lead-Free Double-Perovskite (Elpasolite) Semiconductors: Synthesis and Anion Exchange To Access New Materials. *Nano Lett.* **2018,** *18* (2), 1118-1123.
110. Wu, C.; Zhang, Q.; Liu, Y.; Luo, W.; Guo, X.; Huang, Z.; Ting, H.; Sun, W.; Zhong, X.; Wei, S.; Wang, S.; Chen, Z.; Xiao, L. The Dawn of Lead-Free Perovskite Solar Cell: Highly Stable Double Perovskite $Cs_2AgBiBr_6$ Film. *Adv. Sci.* **2018,** *5* (3), 1700759.
111. Filip, M. R.; Hillman, S.; Haghighirad, A. A.; Snaith, H. J.; Giustino, F. Band Gaps of the Lead-Free Halide Double Perovskites $Cs_2BiAgCl_6$ and $Cs_2BiAgBr_6$ from Theory and Experiment. *J. Phys. Chem. Lett.* **2016,** *7* (13), 2579-2585.
112. Du, K.-z.; Meng, W.; Wang, X.; Yan, Y.; Mitzi, D. B. Bandgap Engineering of Lead-Free Double Perovskite $Cs_2AgBiBr_6$ through Trivalent Metal Alloying. *Angew. Chem. Int. Ed.* **2017,** *56* (28), 8158-8162.
113. Wolf, N. R.; Connor, B. A.; Slavney, A. H.; Karunadasa, H. I. Doubling the Stakes: The Promise of Halide Double Perovskites. *Angew. Chem. Int. Ed.* **2021,** *60* (30), 16264-16278.
114. Slavney, A. H.; Leppert, L.; Bartesaghi, D.; Gold-Parker, A.; Toney, M. F.; Savenije, T. J.; Neaton, J. B.; Karunadasa, H. I. Defect-Induced Band-Edge Reconstruction of a Bismuth-Halide Double Perovskite for Visible-Light Absorption. *J. Am. Chem. Soc.* **2017,** *139* (14), 5015-5018.
115. Lindquist, K. P.; Mack, S. A.; Slavney, A. H.; Leppert, L.; Gold-Parker, A.; Stebbins, J. F.; Salleo, A.; Toney, M. F.; Neaton, J. B.; Karunadasa, H. I. Tuning the bandgap of $Cs_2AgBiBr_6$ through dilute tin alloying. *Chem. Sci.* **2019,** *10* (45), 10620-10628.
116. Song, J.; Xu, L.; Li, J.; Xue, J.; Dong, Y.; Li, X.; Zeng, H. Monolayer and Few-Layer All-Inorganic Perovskites as a New Family of Two-Dimensional Semiconductors for Printable Optoelectronic Devices. *Adv. Mater.* **2016,** *28* (24), 4861-4869.
117. Akın Kara, D.; Kara, K.; Oylumluoglu, G.; Yigit, M. Z.; Can, M.; Kim, J. J.; Burnett, E. K.; Gonzalez Arellano, D. L.; Buyukcelebi, S.; Ozel, F.; Usluer, O.; Briseno, A. L.; Kus, M. Enhanced Device Efficiency and Long-Term Stability via Boronic Acid-Based Self-Assembled Monolayer Modification of Indium Tin Oxide in a Planar Perovskite Solar Cell. *ACS Appl. Mater. Interfaces* **2018,** *10* (35), 30000-30007.

118. Kim, Y.-H.; Cho, H.; Heo, J. H.; Kim, T.-S.; Myoung, N.; Lee, C.-L.; Im, S. H.; Lee, T.-W. Multicolored Organic/Inorganic Hybrid Perovskite Light-Emitting Diodes. *Adv. Mater.* **2015,** *27* (7), 1248-1254.
119. Zhu, X.; Lin, Y.; San Martin, J.; Sun, Y.; Zhu, D.; Yan, Y. Lead halide perovskites for photocatalytic organic synthesis. *Nat. Commun.* **2019,** *10* (1), 2843.
120. Zhu, H.; Fu, Y.; Meng, F.; Wu, X.; Gong, Z.; Ding, Q.; Gustafsson, M. V.; Trinh, M. T.; Jin, S.; Zhu, X. Y. Lead halide perovskite nanowire lasers with low lasing thresholds and high quality factors. *Nat. Mater.* **2015,** *14* (6), 636-642.
121. Tan, Z.-K.; Moghaddam, R. S.; Lai, M. L.; Docampo, P.; Higler, R.; Deschler, F.; Price, M.; Sadhanala, A.; Pazos, L. M.; Credgington, D.; Hanusch, F.; Bein, T.; Snaith, H. J.; Friend, R. H. Bright light-emitting diodes based on organometal halide perovskite. *Nat. Nanotechnol.* **2014,** *9* (9), 687-692.
122. Zhou, H.; Chen, Q.; Li, G.; Luo, S.; Song, T.-b.; Duan, H.-S.; Hong, Z.; You, J.; Liu, Y.; Yang, Y. Interface engineering of highly efficient perovskite solar cells. *Science* **2014,** *345* (6196), 542.
123. Liu, M.; Johnston, M. B.; Snaith, H. J. Efficient planar heterojunction perovskite solar cells by vapour deposition. *Nature* **2013,** *501* (7467), 395-398.
124. Liang, J.; Wang, C.; Wang, Y.; Xu, Z.; Lu, Z.; Ma, Y.; Zhu, H.; Hu, Y.; Xiao, C.; Yi, X.; Zhu, G.; Lv, H.; Ma, L.; Chen, T.; Tie, Z.; Jin, Z.; Liu, J. All-Inorganic Perovskite Solar Cells. *J. Am. Chem. Soc.* **2016,** *138* (49), 15829-15832.
125. Vojvodic, A.; Nørskov, J. K. Optimizing Perovskites for the Water-Splitting Reaction. *Science* **2011,** *334* (6061), 1355.
126. G. Kim, H.; W. Hwang, D.; Kim, J.; G. Kim, Y.; S. Lee, J. Highly donor-doped (110) layered perovskite materials as novel photocatalysts for overall water splitting. *Chem. Commun.* **1999,** (12), 1077-1078.
127. Xu, H.; Zhang, H.; Ma, Y.; Jiang, M.; Zhang, Y.; Wu, Y.; Zhang, H.; Xia, R.; Niu, Q.; Li, X. a.; Huang, W. Morphology control of organic halide perovskites by adding $BiFeO_3$ nanostructures for efficient solar cell. *Sci. Rep.* **2019,** *9* (1), 15441.
128. Cherniukh, I.; Rainò, G.; Stöferle, T.; Burian, M.; Travesset, A.; Naumenko, D.; Amenitsch, H.; Erni, R.; Mahrt, R. F.; Bodnarchuk, M. I.; Kovalenko, M. V. Perovskite-type superlattices from lead halide perovskite nanocubes. *Nature* **2021,** *593* (7860), 535-542.
129. Stoumpos, C. C.; Malliakas, C. D.; Peters, J. A.; Liu, Z.; Sebastian, M.; Im, J.; Chasapis, T. C.; Wibowo, A. C.; Chung, D. Y.; Freeman, A. J.; Wessels, B. W.; Kanatzidis, M. G. Crystal Growth of the Perovskite Semiconductor $CsPbBr_3$: A New Material for High-Energy Radiation Detection. *Cryst. Growth Des.* **2013,** *13* (7), 2722-2727.
130. Zhou, Y.; Zhao, Y. Chemical stability and instability of inorganic halide perovskites. *Energy Environ. Sci.* **2019,** *12*, 1495-1511.
131. Lee, M. M.; Teuscher, J.; Miyasaka, T.; Murakami, T. N.; Snaith, H. J. Efficient Hybrid Solar Cells Based on Meso-Superstructured Organometal Halide Perovskites. *Science* **2012,** *338* (6107), 643.
132. Xiao, Z.; Bi, C.; Shao, Y.; Dong, Q.; Wang, Q.; Yuan, Y.; Wang, C.; Gao, Y.; Huang, J. Efficient, high yield perovskite photovoltaic devices grown by interdiffusion of solution-processed precursor stacking layers. *Energy Environ. Sci.* **2014,** *7* (8), 2619-2623.
133. Holtus, T.; Helmbrecht, L.; Hendrikse, H. C.; Baglai, I.; Meuret, S.; Adhyaksa, G. W. P.; Garnett, E. C.; Noorduin, W. L. Shape-preserving transformation of carbonate minerals into lead halide perovskite semiconductors based on ion exchange/insertion reactions. *Nature Chem.* **2018,** *10* (7), 740-745.

134. Jiang, W.; Pacella, M. S.; Athanasiadou, D.; Nelea, V.; Vali, H.; Hazen, R. M.; Gray, J. J.; McKee, M. D. Chiral acidic amino acids induce chiral hierarchical structure in calcium carbonate. *Nat. Commun.* **2017,** *8* (1), 15066.
135. Chen, Z.; Wang, C.; Zhou, H.; Li, X. Biomimetic Crystallization of Toplike Calcite Single Crystals with an Extensive (00.1) Face in the Presence of Sodium Hyaluronate. *Cryst. Growth Des.* **2010,** *10* (11), 4722-4727.
136. Morse, J. W.; Arvidson, R. S.; Lüttge, A. Calcium Carbonate Formation and Dissolution. *Chem. Rev.* **2007,** *107* (2), 342-381.
137. Walker, J. M.; Marzec, B.; Nudelman, F. Solid-State Transformation of Amorphous Calcium Carbonate to Aragonite Captured by CryoTEM. *Angew. Chem. Int. Ed.* **2017,** *56* (39), 11740-11743.
138. Zhang, Z.; Xie, Y.; Xu, X.; Pan, H.; Tang, R. Transformation of amorphous calcium carbonate into aragonite. *J. Cryst. Growth* **2012,** *343* (1), 62-67.
139. Yuan, K.; Lee, S. S.; De Andrade, V.; Sturchio, N. C.; Fenter, P. Replacement of Calcite ($CaCO_3$) by Cerussite ($PbCO_3$). *Environ. Sci. Technol.* **2016,** *50* (23), 12984-12991.
140. Kim, Y.; Abdilla, B.; Yuan, K.; De Andrade, V.; Sturchio, N. C.; Lee, S. S.; Fenter, P. Replacement of Calcium Carbonate Polymorphs by Cerussite. *ACS Earth Space Chem.* **2021,** *5* (9), 2433-2441.
141. Putnis, A. Mineral Replacement Reactions. *Rev. Mineral. Geochem.* **2009,** *70* (1), 87-124.
142. Putnis, A. Mineral replacement reactions: from macroscopic observations to microscopic mechanisms. *Mineral. Mag.* **2018,** *66* (5), 689-708.
143. Yuan, K.; Starchenko, V.; Lee, S. S.; De Andrade, V.; Gursoy, D.; Sturchio, N. C.; Fenter, P. Mapping Three-dimensional Dissolution Rates of Calcite Microcrystals: Effects of Surface Curvature and Dissolved Metal Ions. *ACS Earth Space Chem.* **2019,** *3* (5), 833-843.
144. Gao, Y.; Wu, Y.; Lu, H.; Chen, C.; Liu, Y.; Bai, X.; Yang, L.; Yu, W. W.; Dai, Q.; Zhang, Y. $CsPbBr_3$ perovskite nanoparticles as additive for environmentally stable perovskite solar cells with 20.46% efficiency. *Nano Energy* **2019,** *59*, 517-526.
145. Swarnkar, A.; Chulliyil, R.; Ravi, V. K.; Irfanullah, M.; Chowdhury, A.; Nag, A. Colloidal $CsPbBr_3$ Perovskite Nanocrystals: Luminescence beyond Traditional Quantum Dots. *Angew. Chem. Int. Ed.* **2015,** *54* (51), 15424-15428.
146. Wang, Y.; Guan, X.; Li, D.; Cheng, H.-C.; Duan, X.; Lin, Z.; Duan, X. Chemical vapor deposition growth of single-crystalline cesium lead halide microplatelets and heterostructures for optoelectronic applications. *Nano Res.* **2017,** *10* (4), 1223-1233.
147. Gibson, N. A.; Koscher, B. A.; Alivisatos, A. P.; Leone, S. R. Excitation Intensity Dependence of Photoluminescence Blinking in $CsPbBr_3$ Perovskite Nanocrystals. *J. Phys. Chem. C* **2018,** *122* (22), 12106-12113.
148. Behera, T.; Pathoor, N.; Phadnis, C.; Buragohain, S.; Chowdhury, A. Spatially correlated photoluminescence blinking and flickering of hybrid-halide perovskite micro-rods. *J. Lumin.* **2020,** *223*, 117202.
149. Nirmal, M.; Dabbousi, B. O.; Bawendi, M. G.; Macklin, J. J.; Trautman, J. K.; Harris, T. D.; Brus, L. E. Fluorescence intermittency in single cadmium selenide nanocrystals. *Nature* **1996,** *383* (6603), 802-804.
150. Li, Q.; Lian, T. Area- and Thickness-Dependent Biexciton Auger Recombination in Colloidal CdSe Nanoplatelets: Breaking the "Universal Volume Scaling Law". *Nano Lett.* **2017,** *17* (5), 3152-3158.

151. Frantsuzov, P.; Kuno, M.; Jankó, B.; Marcus, R. A. Universal emission intermittency in quantum dots, nanorods and nanowires. *Nat. Phys.* **2008,** *4* (7), 519-522.
152. Tong, G.; Chen, T.; Li, H.; Qiu, L.; Liu, Z.; Dang, Y.; Song, W.; Ono, L. K.; Jiang, Y.; Qi, Y. Phase transition induced recrystallization and low surface potential barrier leading to 10.91%-efficient $CsPbBr_3$ perovskite solar cells. *Nano Energy* **2019,** *65*, 104015.
153. Zhang, J.; Wang, Q.; Zhang, X.; Jiang, J.; Gao, Z.; Jin, Z.; Liu, S. High-performance transparent ultraviolet photodetectors based on inorganic perovskite $CsPbCl_3$ nanocrystals. *RSC Adv.* **2017,** *7* (58), 36722-36727.
154. Milstein, T. J.; Kroupa, D. M.; Gamelin, D. R. Picosecond Quantum Cutting Generates Photoluminescence Quantum Yields Over 100% in Ytterbium-Doped $CsPbCl_3$ Nanocrystals. *Nano Lett.* **2018,** *18* (6), 3792-3799.
155. Behera, R. K.; Das Adhikari, S.; Dutta, S. K.; Dutta, A.; Pradhan, N. Blue-Emitting $CsPbCl_3$ Nanocrystals: Impact of Surface Passivation for Unprecedented Enhancement and Loss of Optical Emission. *J. Phys. Chem. Lett.* **2018,** *9* (23), 6884-6891.
156. Akkerman, Q. A.; Meggiolaro, D.; Dang, Z.; De Angelis, F.; Manna, L. Fluorescent Alloy $CsPb_xMn_{1-x}I_3$ Perovskite Nanocrystals with High Structural and Optical Stability. *ACS Energy Lett.* **2017,** *2* (9), 2183-2186.
157. Dutta, A.; Dutta, S. K.; Das Adhikari, S.; Pradhan, N. Phase-Stable $CsPbI_3$ Nanocrystals: The Reaction Temperature Matters. *Angew. Chem. Int. Ed.* **2018,** *57* (29), 9083-9087.
158. Lu, M.; Zhang, X.; Zhang, Y.; Guo, J.; Shen, X.; Yu, W. W.; Rogach, A. L. Simultaneous Strontium Doping and Chlorine Surface Passivation Improve Luminescence Intensity and Stability of $CsPbI_3$ Nanocrystals Enabling Efficient Light-Emitting Devices. *Adv. Mater.* **2018,** *30* (50), 1804691.
159. Wang, B.; Navrotsky, A. Thermodynamics of cesium lead halide ($CsPbX_3$, x= I, Br, Cl) perovskites. *Thermochim. Acta* **2021,** *695*, 178813.
160. Liu, J.; Song, K.; Zheng, X.; Yin, J.; Yao, K. X.; Chen, C.; Yang, H.; Hedhili, M. N.; Zhang, W.; Han, P.; Mohammed, O. F.; Han, Y.; Bakr, O. M. Cyanamide Passivation Enables Robust Elemental Imaging of Metal Halide Perovskites at Atomic Resolution. *J. Phys. Chem. Lett.* **2021**, 10402-10409.
161. Hutter, E. M.; Gélvez-Rueda, M. C.; Osherov, A.; Bulović, V.; Grozema, F. C.; Stranks, S. D.; Savenije, T. J. Direct–indirect character of the bandgap in methylammonium lead iodide perovskite. *Nat. Mater.* **2017,** *16* (1), 115-120.
162. Kim, H.; Lim, K.-G.; Lee, T.-W. Planar heterojunction organometal halide perovskite solar cells: roles of interfacial layers. *Energy Environ. Sci.* **2016,** *9* (1), 12-30.
163. Ren, H.; Yu, S.; Chao, L.; Xia, Y.; Sun, Y.; Zuo, S.; Li, F.; Niu, T.; Yang, Y.; Ju, H.; Li, B.; Du, H.; Gao, X.; Zhang, J.; Wang, J.; Zhang, L.; Chen, Y.; Huang, W. Efficient and stable Ruddlesden–Popper perovskite solar cell with tailored interlayer molecular interaction. *Nat. Photonics* **2020,** *14* (3), 154-163.
164. Shamsi, J.; Urban, A. S.; Imran, M.; De Trizio, L.; Manna, L. Metal Halide Perovskite Nanocrystals: Synthesis, Post-Synthesis Modifications, and Their Optical Properties. *Chem. Rev.* **2019,** *119* (5), 3296-3348.
165. Wang, T.; Yan, F. Reducing Agents for Improving the Stability of Sn-based Perovskite Solar Cells. *Chem. Asian. J.* **2020,** *15* (10), 1524-1535.
166. Khalfin, S.; Bekenstein, Y. Advances in lead-free double perovskite nanocrystals, engineering band-gaps and enhancing stability through composition tunability. *Nanoscale* **2019,** *11* (18), 8665-8679.

167. Wells, H. L. Some complex chlorides containing gold. *Am. J. Sci.* **1922,** *s5-3* (17), 315.
168. Slavney, A. H.; Smaha, R. W.; Smith, I. C.; Jaffe, A.; Umeyama, D.; Karunadasa, H. I. Chemical Approaches to Addressing the Instability and Toxicity of Lead–Halide Perovskite Absorbers. *Inorg. Chem.* **2017,** *56* (1), 46-55.
169. Dahl, J. C.; Osowiecki, W. T.; Cai, Y.; Swabeck, J. K.; Bekenstein, Y.; Asta, M.; Chan, E. M.; Alivisatos, A. P. Probing the Stability and Band Gaps of $Cs_2AgInCl_6$ and $Cs_2AgSbCl_6$ Lead-Free Double Perovskite Nanocrystals. *Chem. Mater.* **2019,** *31* (9), 3134-3143.
170. Bekenstein, Y.; Dahl, J. C.; Huang, J.; Osowiecki, W. T.; Swabeck, J. K.; Chan, E. M.; Yang, P.; Alivisatos, A. P. The Making and Breaking of Lead-Free Double Perovskite Nanocrystals of Cesium Silver–Bismuth Halide Compositions. *Nano Lett.* **2018,** *18* (6), 3502-3508.
171. Lee, W.; Hong, S.; Kim, S. Colloidal Synthesis of Lead-Free Silver–Indium Double-Perovskite $Cs_2AgInCl_6$ Nanocrystals and Their Doping with Lanthanide Ions. *J. Phys. Chem. C* **2019,** *123* (4), 2665-2672.
172. Tanner, P. A.; Duan, C.-K.; Cheng, B.-M. Excitation and Emission Spectra of $Cs_2NaLnCl_6$ Crystals Using Synchrotron Radiation. *Spectrosc. Lett.* **2010,** *43* (5), 431-445.
173. Barbanel', Y. A.; Chudnovskaya, G. P.; Dushin, R. B.; Kolin, V. V.; Kotlin, V. P.; Nekhoroshkov, S. N.; Pen'kin, M. V. Optical Spectra and Crystal Field of Am^{3+} and Cm^{3+} in the Cubic Elpasolite Crystals. *Radiochim. Acta* **1997,** *78* (s1), 69-72.
174. Schwartz, R. W. Electronic structure of the octahedral hexachloroytterbate ion. *Inorg. Chem.* **1977,** *16* (7), 1694-1698.
175. Chen, M.; Zou, Y.; Wu, L.; Pan, Q.; Yang, D.; Hu, H.; Tan, Y.; Zhong, Q.; Xu, Y.; Liu, H.; Sun, B.; Zhang, Q. Solvothermal Synthesis of High-Quality All-Inorganic Cesium Lead Halide Perovskite Nanocrystals: From Nanocube to Ultrathin Nanowire. *Adv. Funct. Mater.* **2017,** *27* (23), 1701121.
176. Grisorio, R.; Conelli, D.; Giannelli, R.; Fanizza, E.; Striccoli, M.; Altamura, D.; Giannini, C.; Allegretta, I.; Terzano, R.; Suranna, G. P. A new route for the shape differentiation of cesium lead bromide perovskite nanocrystals with near-unity photoluminescence quantum yield. *Nanoscale* **2020,** *12* (32), 17053-17063.
177. Yao, M.-M.; Wang, L.; Yao, J.-S.; Wang, K.-H.; Chen, C.; Zhu, B.-S.; Yang, J.-N.; Wang, J.-J.; Xu, W.-P.; Zhang, Q.; Yao, H.-B. Improving Lead-Free Double Perovskite $Cs_2NaBiCl_6$ Nanocrystal Optical Properties via Ion Doping. *Adv. Opt. Mater.* **2020,** *8* (8), 1901919.
178. Wu, H.; Erbing, A.; Johansson, M. B.; Wang, J.; Kamal, C.; Odelius, M.; Johansson, E. M. J. Mixed-Halide Double Perovskite Cs_2AgBiX_6 (X=Br, I) with Tunable Optical Properties via Anion Exchange. *ChemSusChem* **2021,** *14* (20), 4507-4515.
179. Kumar, A.; Swami, S. K.; Rawat, S. S.; Singh, V. N.; Sinha, O. P.; Srivastava, R. Mixed bismuth-antimony-based double perovskite nanocrystals for solar cell application. *Int. J. Energy Res.* **2021,** *45* (11), 16769-16780.

Appendix

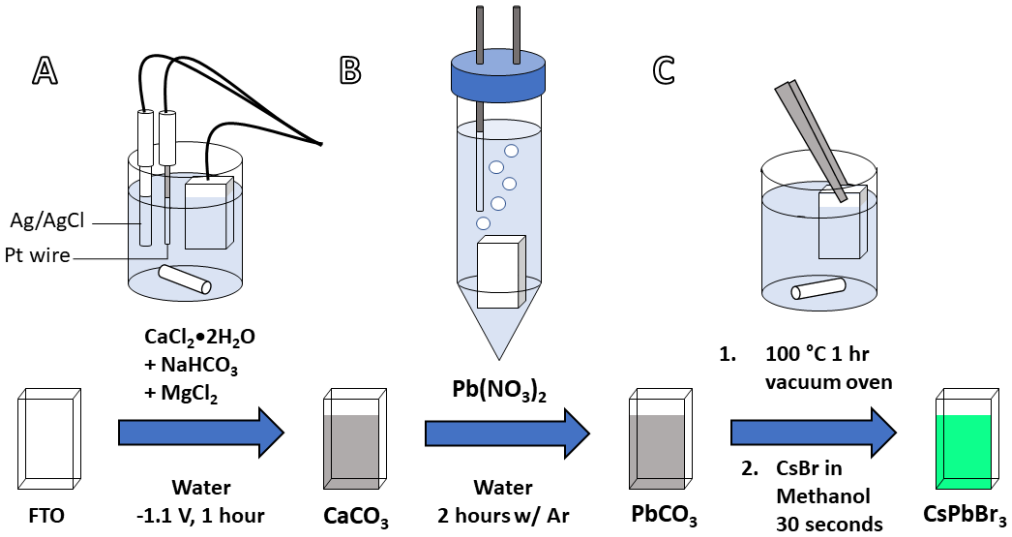

Figure A1. Reaction scheme for the electrochemical deposition of $CaCO_3$ and subsequent conversion to perovskite $CsPbBr_3$ via ion exchange reactions. (A) Experimental setup for electrochemical deposition of $CaCO_3$ on FTO. (B) $CaCO_3$ microstructures are left in an airtight vessel, a centrifuge tube with two holes pierced through its cap, while Ar gas is sparged through the reaction solution. (C) After being dried in a vacuum oven for 1 hour, the sample is held by forceps in the reaction mixture for 30 seconds.

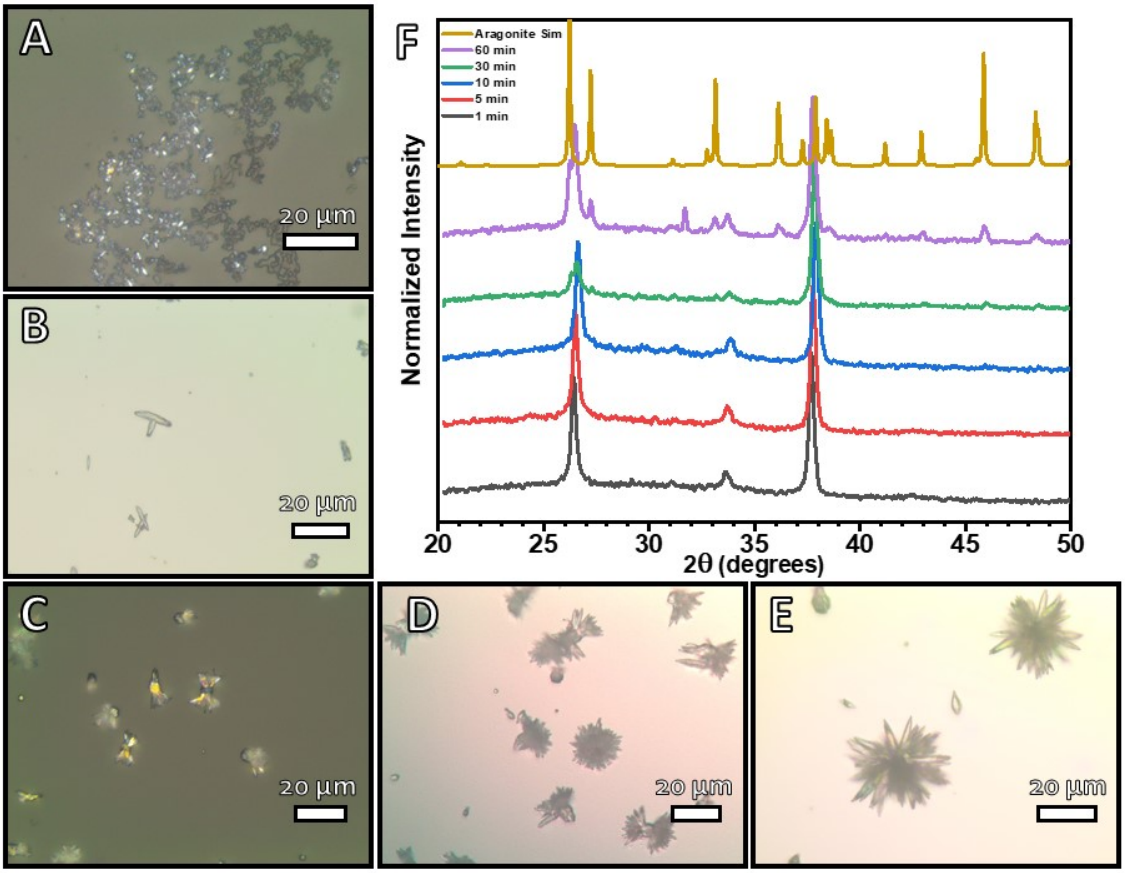

Figure A2. Optical microscope images taken at 40× magnification of $CaCO_3$ crystallites electrochemically deposited for (A) 1, (B) 5, (C) 10, (D) 30, and (E) 60 minutes on FTO with (F) their respective powder X-ray diffraction (PXRD) patterns.

$CaCO_3$			$PbCO_3$			$CsPbBr_3$		
Element	**Atomic %**	**Expected Atomic %**	**Element**	**Atomic %**	**Expected Atomic %**	**Element**	**Atomic %**	**Expected Atomic %**
C	**20.1**	**20**	**C**	**34.7**	**20**	**C**	**25.5**	**0**
O	**60.9**	**60**	**O**	**51.9**	**60**	**O**	**52.9**	**0**
Ca	**17.5**	**20**	**Ca**	**0**	**0**	**Ca**	**3.0**	**0**
Pb	**0**	**0**	**Pb**	**13.3**	**20**	**Pb**	**10.5**	**20**
Cs	**0**	**0**	**Cs**	**0**	**0**	**Cs**	**3.8**	**20**
Br	**0**	**0**	**Br**	**0**	**0**	**Br**	**4.1**	**60**

Table A1. SEM-EDS elemental composition analysis of microstructures after electrochemical deposition of $CaCO_3$ and conversion to $PbCO_3$ and $CsPbBr_3$.

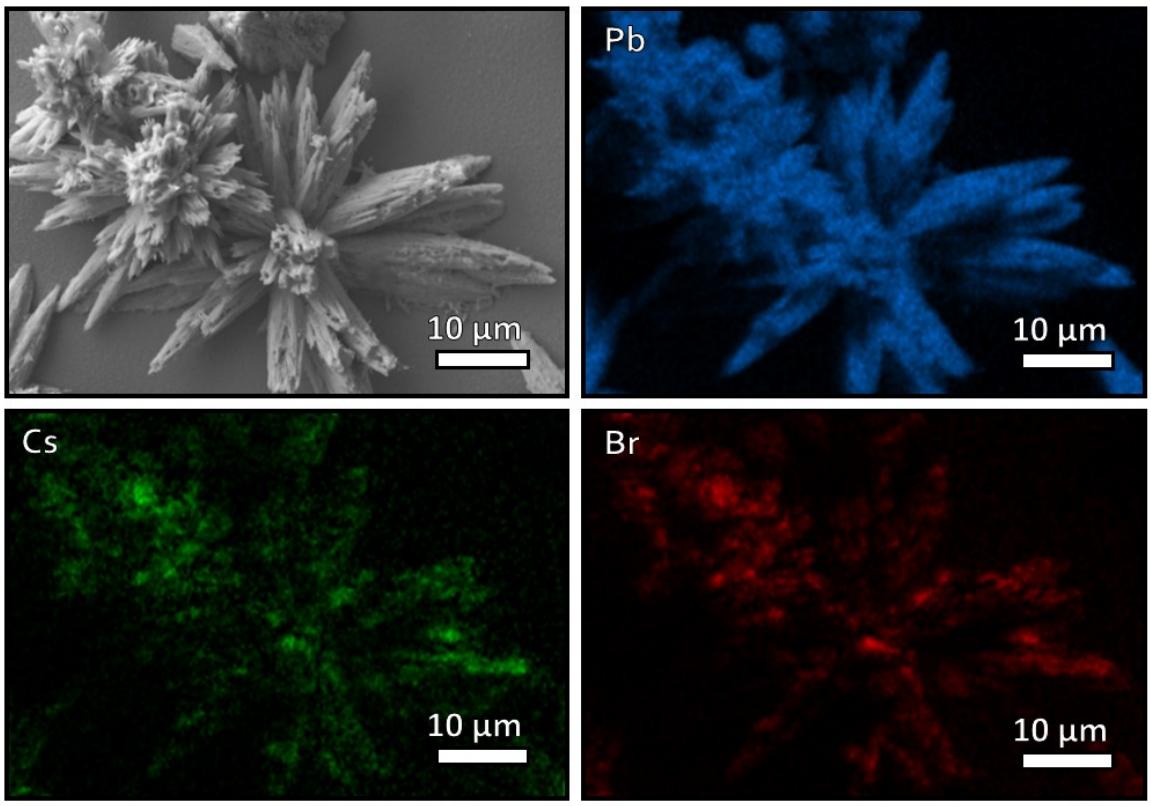

Figure A3. SEM micrograph of fully converted microstructure (top left) with EDS map analyses of Pb, Cs, and Br. Mapping analysis of Pb in Figure A3 shows a clear picture of Pb residing in the microstructure. Analyses of Cs and Br show similar results, but to a less intense degree. Though it is a fainter signal compared to that of Pb, Cs and Br can be seen in the microstructure as well.

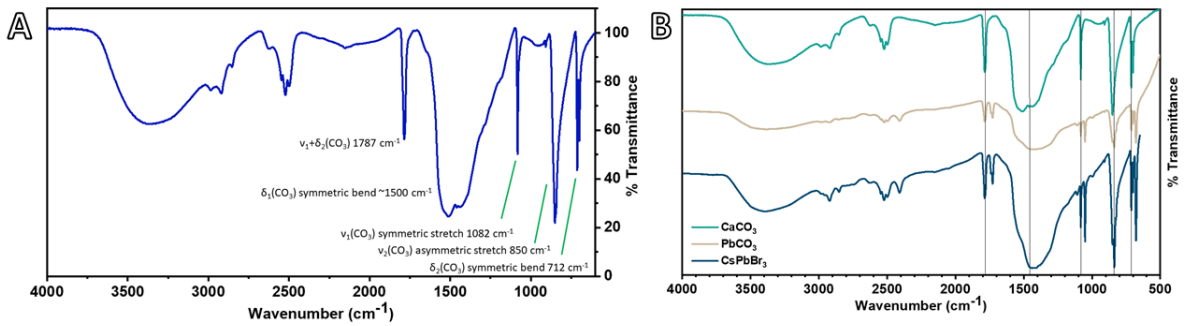

Figure A4. Diffuse reflectance infrared Fourier transform spectroscopic data for (A) electrochemically deposited $CaCO_3$ microstructures with peak assignments and (B) as-deposited $CaCO_3$ compared to microstructures converted to $PbCO_3$ and $CsPbBr_3$. The subsequent traces in Figure A4B, taken after conversion to $PbCO_3$ and $CsPbBr_3$, contain the same peaks as seen in the spectrum of $CaCO_3$, but also show a secondary set of peaks slightly red shifted in energy. This occurs because of the formation of a core/shell structure where the electrochemically deposited $CaCO_3$ microstructures are converted to $PbCO_3$ up to a certain depth but not completely. As such, both $CaCO_3$ and $PbCO_3$ exist in the sample after exposure to the concentrated $Pb(NO_3)_2$ aqueous solution, and this is reflected in the results shown in Figure A4. The $CsPbBr_3$ trace looks identical to that of $PbCO_3$ as the amount of $PbCO_3$ that has been converted to $CsPbBr_3$ is likely too small to have caused any changes in the IR spectrum of the final material. This demonstrates the lack of surface sensitivity of DRIFTS and the need for more sensitive methods of characterization.

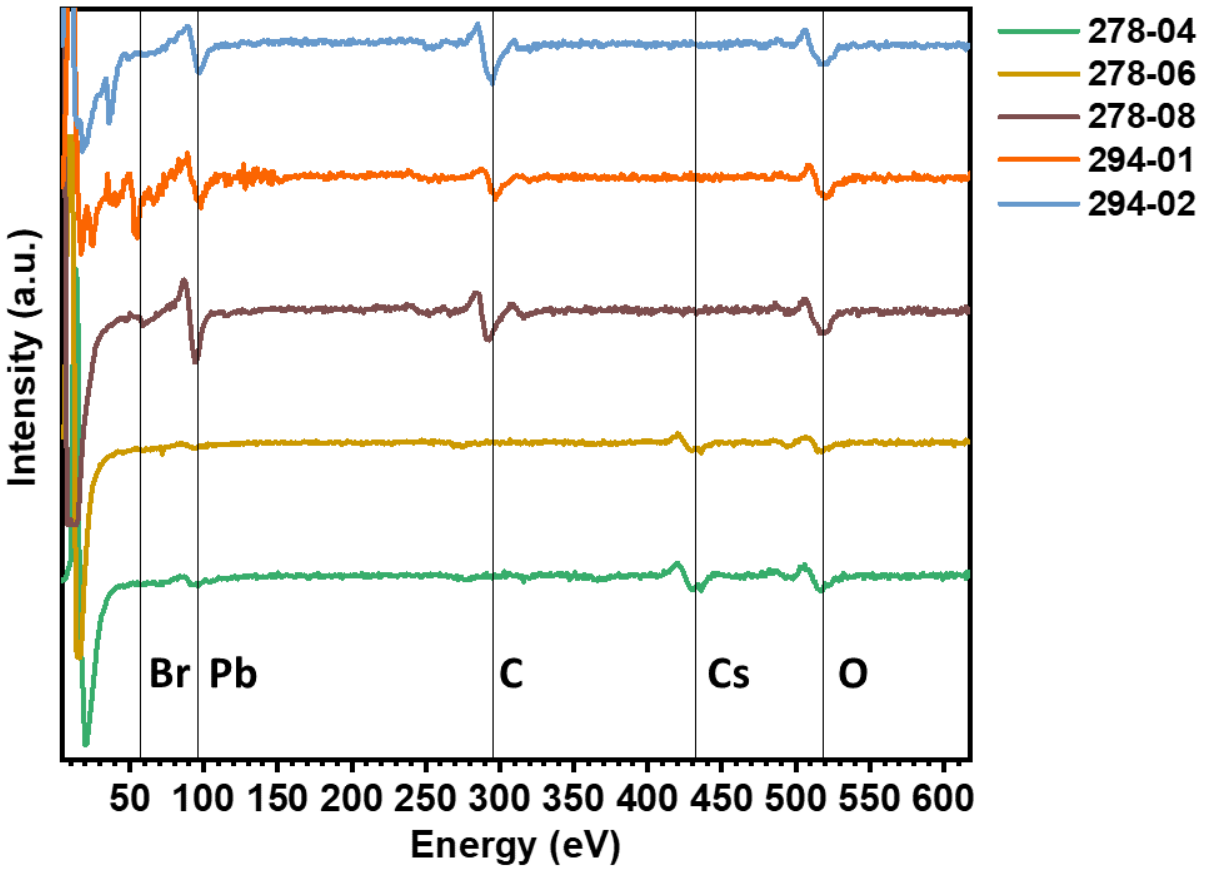

Figure A5. Auger Electron Spectroscopic (AES) data taken from various points on two different samples with characteristic energies outlined and labelled for Br, Pb, C, Cs, and O. Samples are numbered 278 and 294 and were analyzed at different positions on the samples. These different analyses are denoted as run numbers after the sample number in the legend of Figure A5.

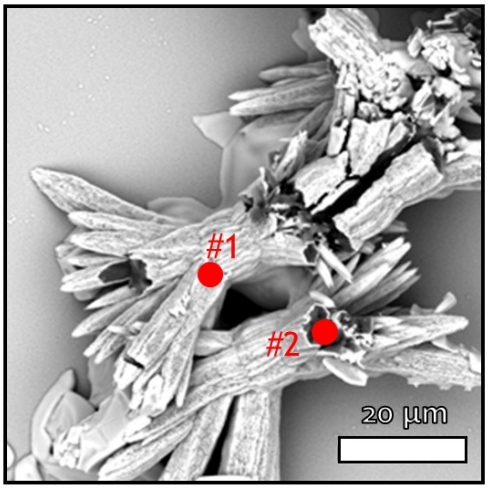

Spot#1

Element	Atomic%	Expected Atomic%
O	50.14	0
C	22.61	0
Pb	18.87	20
Ca	7.01	0
Cs	0.71	20
Br	0.67	60

Spot#2

Element	Atomic%	Expected Atomic%
O	56.08	60
C	22.61	20
Pb	20.53	20
Ca	0.33	0
Cs	0.25	0
Br	0.20	0

Figure A6. Secondary electron scanning mode SEM micrograph of fully converted, fractured microstructure with accompanying SEM-EDS analysis of surface and exposed interior.

Sample ID	[Ca](ppm)	[Br](ppm)	[Cs](ppm)	[Pb](ppm)	Br:Cs by element mass
299	4.20E-01	4.38E-02	2.54E-02	1.20E+00	2.87
306	4.26E-01	3.21E-02	8.55E-03	1.20E+00	6.24
302	1.17E-01	3.32E-02	1.91E-02	3.76E-01	2.89
309	1.38E-01	3.22E-02	9.18E-03	7.61E-01	5.83
Stock 1	8.41E-03	8.78E-03	0.00E+00	1.31E-02	
Stock 2	6.43E-03	4.81E-03	0.00E+00	0.00E+00	
Stock 3	1.74E-02	2.90E-03	0.00E+00	3.44E-03	

Table A2. Chemical composition of perovskite microstructure samples as determined by inductively coupled plasma – mass spectrometry (ICP-MS) compared to elemental concentrations present in stock digestion solution. The data reported in Table A2 show some contamination in the stock digestion solution of Ca, Br, and Pb. The differences between the stock solution and the actual sample analyses, however, were found to be at least one order of magnitude, meaning the amounts present in the samples are significantly different from those in the stock digestion solution. The samples named “Stock 1, 2, and 3” are different aliquots analyzed from the same stock solution. Each sample was run as an individual batch.

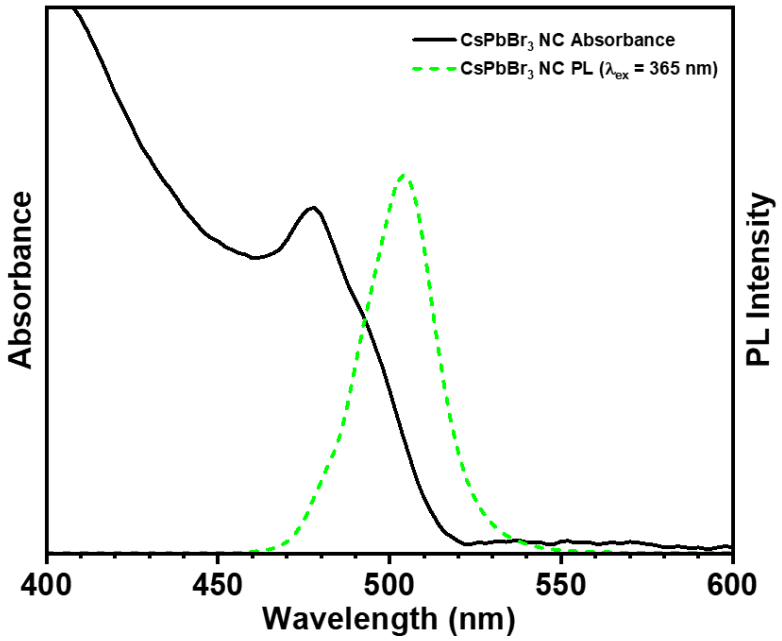

Figure A7. Absorbance and PL spectra acquired for as-synthesized $CsPbBr_3$ nanocrystals suspended in toluene.

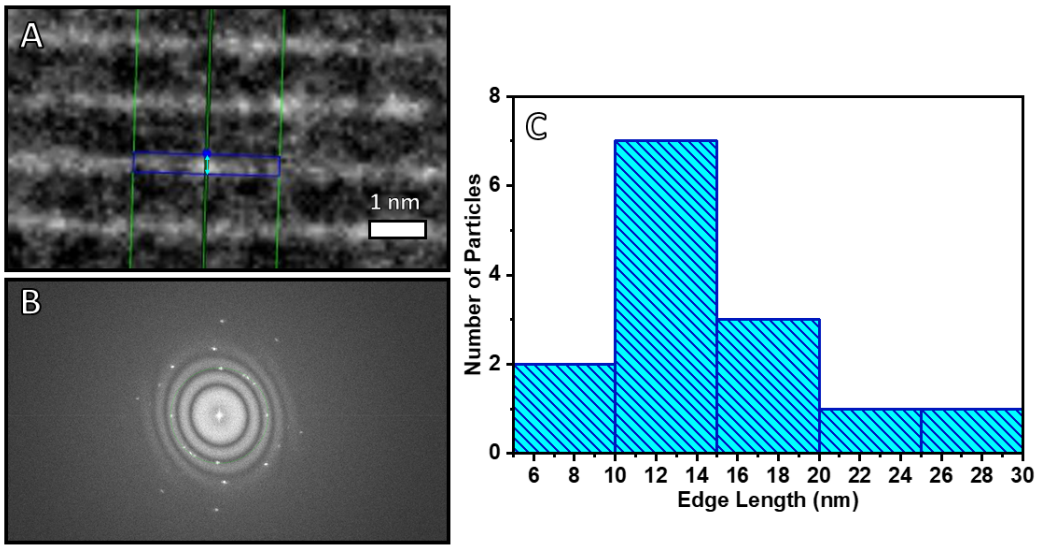

Figure A8. (A) Measurement of interplanar spacing (d-spacing) for (210) crystal plane in bright field TEM depicted by light blue arrow. (B) Fast Fourier transform (FFT) collected of observed nanoparticle. (C) Histogram of nanoparticle size.

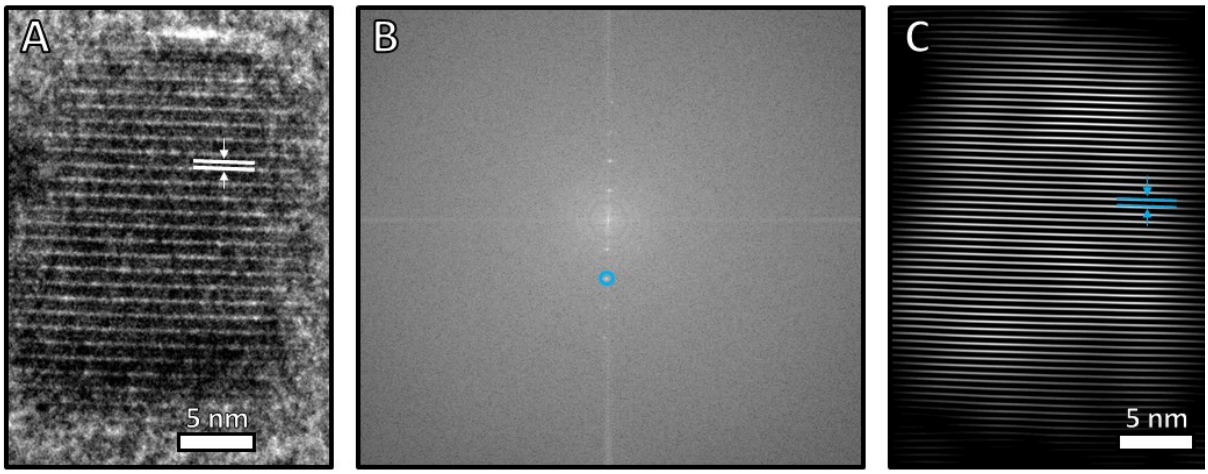

Figure A9. (A) Measurement of interplanar spacing (d-spacing) for (100) crystal plane in bright field TEM depicted by space between white lines. (B) Fast Fourier transform (FFT) calculated for observed nanoparticle. (C) Inverted FFT and interplanar d-spacing measurement of (100) crystal plane.

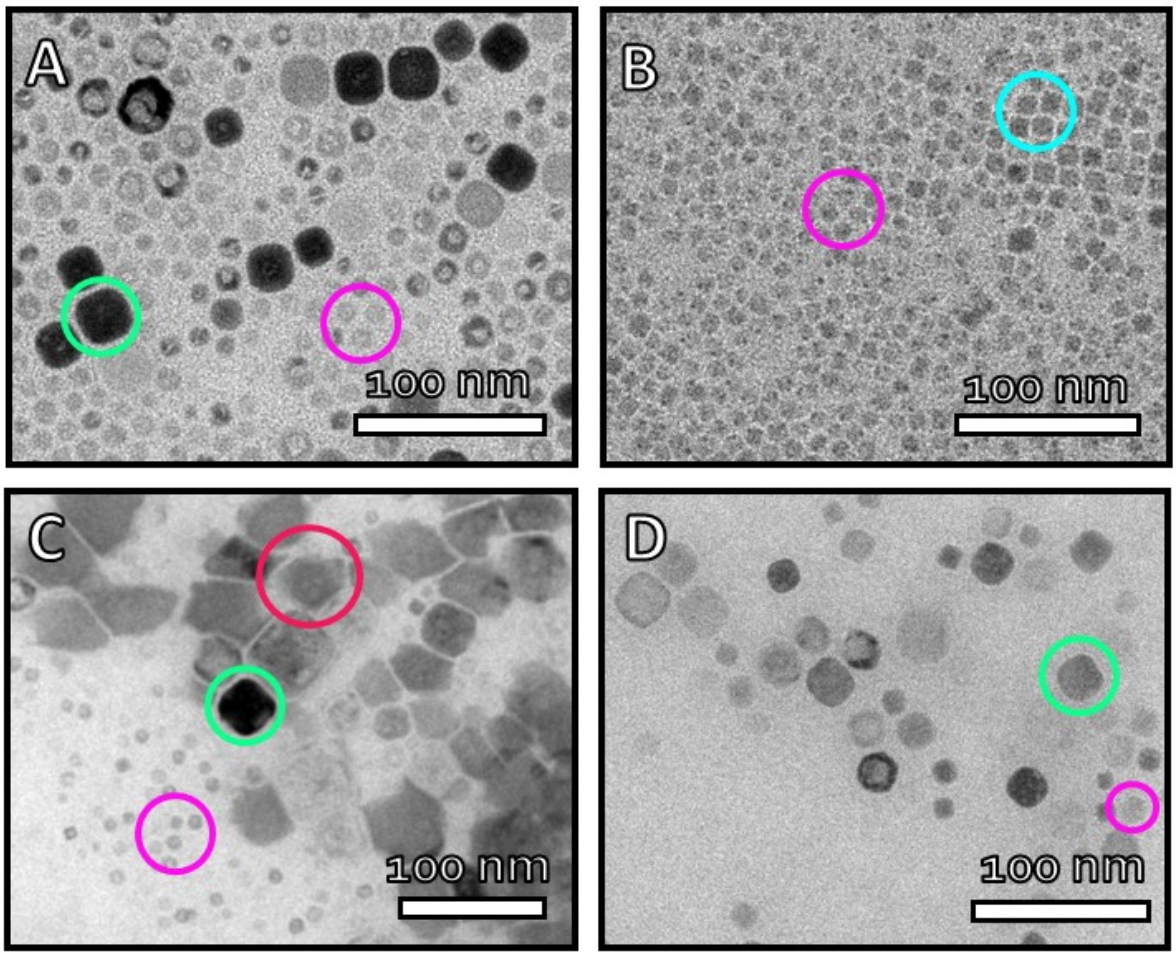

Figure A10: Zoomed-in transmission electron micrographs of (A) 5-second, (B) 1-, (C) 5-, and (D) 10-minute reaction samples shown in Figure 3.1 with different observed morphologies highlighted. Hexahedral, cubic, spherical, and amorphous particles are highlighted by green, blue, purple, and red circles, respectively.

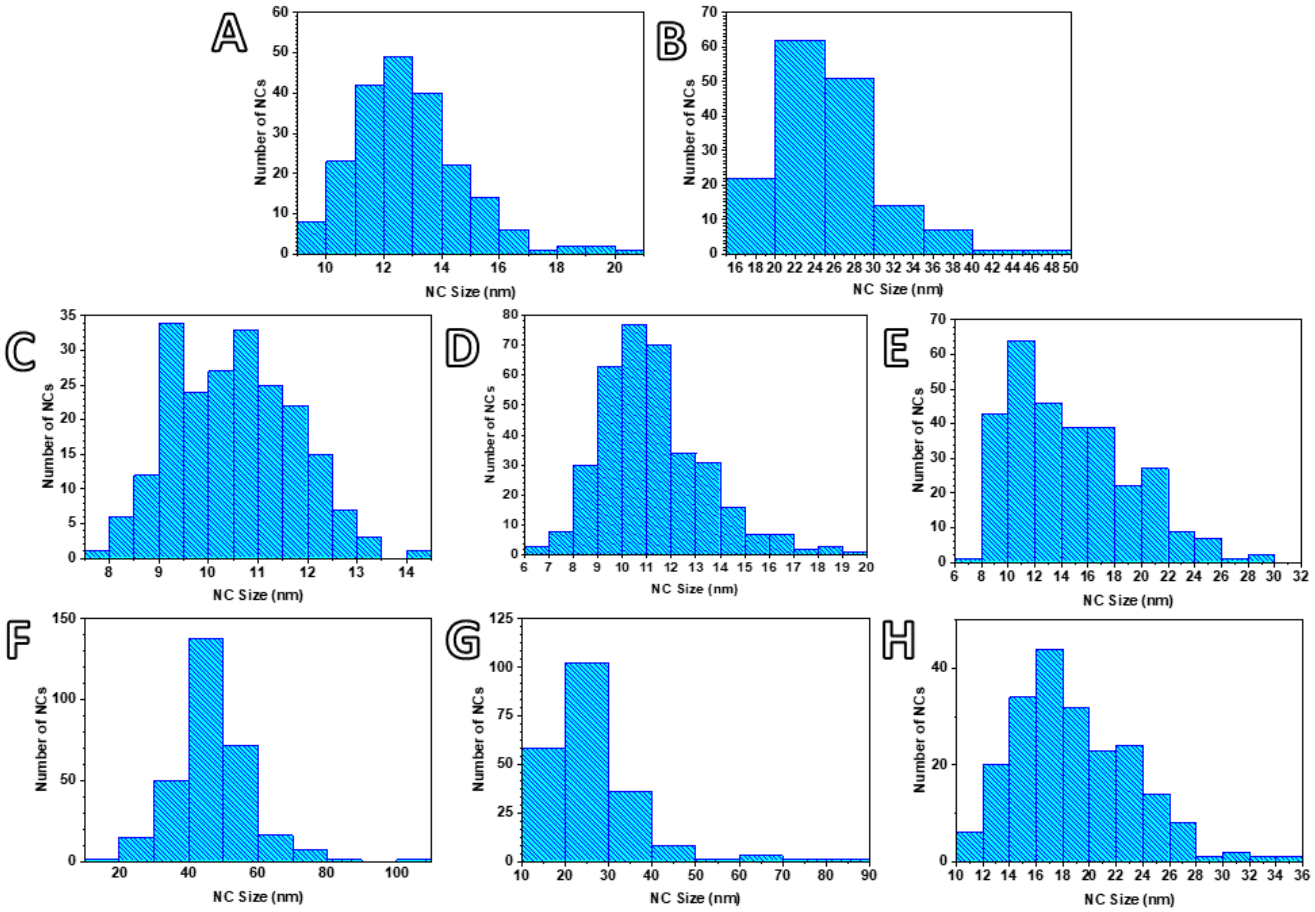

Figure A11: Histograms (A, B) represent the size distributions of small spherical NCs and hexahedron NCs present in the 5-second sample, respectively. Histograms (C, D) represent the size distributions of small spherical NCs and cubic NCs present in the 1-minute sample, respectively. Histograms (E, F) represent the size distributions of large amorphous particles and smaller spherical and cuboid NCs present in 5-minute sample, respectively. Histograms (G, H) represent the size distribution of hexahedral NCs and spherical NCs present in the 10-minute sample, respectively.